JGR Oceans

RESEARCH ARTICLE
10.1029/2024JC022122

Freshwater Sources in the Global Ocean Through Salinity-$\delta^{18}O$ Relationships: A Machine Learning Solution to a Water Mass Problem

Xabier Davila[1,2], Elaine L. McDonagh[1,2,3], Fatma Jebri[3], Geoffrey Gebbie[4], and Michael P. Meredith[5]

[1]NORCE Research AS, Bergen, Norway, [2]Bjerknes Centre for Climate Research, Bergen, Norway, [3]National Oceanography Centre, Southampton, UK, [4]Department of Physical Oceanography, Woods Hole Oceanographic Institution, Woods Hole, MA, USA, [5]British Antarctic Survey, Cambridge, UK

Key Points:

- This study quantifies meteoric water and sea ice meltwater in the ocean freshwater budget by estimating multiple freshwater endmembers
- $\delta^{18}O$ shows that Antarctic bottom water has significantly freshened as a result of decreasing sea ice formation
- The freshwater budget for the interior ocean is asymmetric between hemispheres due to the different role of sea ice processes

Supporting Information:

Supporting Information may be found in the online version of this article.

Correspondence to:

X. Davila,
xada@norceresearch.no

Citation:

Davila, X., McDonagh, E. L., Jebri, F., Gebbie, G., & Meredith, M. P. (2025). Freshwater sources in the global ocean through salinity-$\delta^{18}O$ relationships: A machine learning solution to a water mass problem. *Journal of Geophysical Research: Oceans*, *130*, e2024JC022122. https://doi.org/10.1029/2024JC022122

Received 13 NOV 2024
Accepted 22 AUG 2025

Author Contributions:

Conceptualization: Xabier Davila, Elaine L. McDonagh, Geoffrey Gebbie, Michael P. Meredith
Data curation: Xabier Davila, Michael P. Meredith
Formal analysis: Xabier Davila, Elaine L. McDonagh, Fatma Jebri, Michael P. Meredith
Funding acquisition: Elaine L. McDonagh
Investigation: Xabier Davila
Methodology: Xabier Davila, Elaine L. McDonagh, Fatma Jebri, Geoffrey Gebbie, Michael P. Meredith
Project administration: Elaine L. McDonagh

Abstract Changes in the hydrological cycle can affect ocean circulation and ventilation. Freshwater enters the ocean as meteoric water (MW; precipitation, river runoff, and glacial discharge) and sea ice meltwater (SIM). These inputs are traced using seawater salinity and stable oxygen isotopes in seawater, $\delta^{18}O$. We apply a self-organizing map, a machine learning technique, to water mass properties to estimate the global distribution of the isotopic signature of MW ($\delta^{18}O_{MW}$) by characterizing distinct salinity-$\delta^{18}O$ relationships from two comprehensive data sets. The inferred $\delta^{18}O_{MW}$ is then used in a three-endmember mixing model to provide a globally coherent MW and SIM contributions to the extratropical ocean freshwater budget. Through the use of $\delta^{18}O$, our results show the role of MW and SIM in dense water formation and the resulting interhemispheric asymmetry in the freshwater sources that fill the interior ocean freshwater budget. Trends drawn in θ-S space show a significant decrease in sea ice formation driving the freshening of Antarctic bottom water for the 1980–2023 period, whereas SIM is significantly increasing in parts of the Arctic halocline. The different roles of sea ice in dense water formation has implications for future ocean circulation under climate change, where machine learning techniques applied to $\delta^{18}O$ have been proven to have utility in detecting such changes.

Plain Language Summary Understanding where freshwater in the ocean is coming from is important for studying changes in ocean circulation and climate change. Freshwater enters the ocean mainly through rain and snow, rivers, melting glaciers, and melting sea ice. In this study, we used a machine learning method to better understand how freshwater from rain and river runoff (called meteoric water) and from melting sea ice spreads through the ocean. We combined global data to estimate how much of each type of freshwater is present in different parts of the ocean. In the Southern Ocean around Antarctica, we found that a reduction in sea ice formation is making deep waters fresher. In the Arctic, sea ice meltwater is increasing in surface layers. The sources filling the freshwater budget are different between the Northern and Southern Hemispheres, mainly because sea ice plays different roles in the formation of deep ocean waters.

1. Introduction

At climate relevant timescales, the interior ocean can only receive freshwater at its surface through inputs of (a) meteorological precipitation, also known as meteoric water (MW), which also includes river runoff and discharge from glaciers and ice sheets, and (b) sea ice meltwater (SIM). Freshwater loss occurs through evaporation, and sea ice formation with associated brine rejection. These processes have an important role in climate and its variability as changes in salinity affect ocean circulation and ventilation (De Lavergne et al., 2014; Biló et al., 2022; Nelson et al., 2024), which in turns affects carbon and heat uptake through their tight link (Davila et al., 2022; Newsom et al., 2020). High-latitude water masses in both the northern and southern hemisphere have experienced changes regarding their freshwater content over the observational record (Holliday et al., 2008; Zhou et al., 2023). Although determining the fluxes of both MW and SIM to the freshwater budget is critical, their quantification through direct measurement is challenging. Their net effect, however, can be traced through changes in salinity and the stable isotope composition of seawater. This possibility stems from the strong linear relationship between salinity and $\delta^{18}O$ (the relative abundance of the molecule with the heavier oxygen-18 isotope compared with that of the lighter and more abundant oxygen-16 isotope) (Craig & Gordon, 1965). Because addition/removal of water through MW and SIM pulls this relationship in different directions, the contribution of each of these freshwater sources can be quantified through a simple three-endmember mixing model (Figure 1), subjected to suitable

Resources: Xabier Davila, Elaine L. McDonagh
Software: Fatma Jebri
Supervision: Elaine L. McDonagh
Validation: Xabier Davila, Geoffrey Gebbie, Michael P. Meredith
Visualization: Xabier Davila
Writing – original draft: Xabier Davila
Writing – review & editing: Xabier Davila, Elaine L. McDonagh, Fatma Jebri, Geoffrey Gebbie, Michael P. Meredith

assumptions (Östlund & Hut, 1984). A critical step in this framework is defining the endmember properties, particularly the MW endmember $\delta^{18}O$ composition $(\delta^{18}O_{MW})$, which varies regionally. Until now, the studies that have utilized this framework have defined a single $\delta^{18}O_{MW}$ as endmember, which limits its applications to a regional scale (e.g., Bauch et al., 1995, 2005; Hennig et al., 2024; Meredith et al., 2018) and hinders a globally coherent quantitative view of the contribution of MW and SIM to the ocean freshwater budget. In this study we aim to first characterize $\delta^{18}O_{MW}$ globally and then apply the three-endmember mixing model to estimate the MW and SIM contributions to polar and subpolar water masses.

The strong linear relationship of salinity and $\delta^{18}O$ is widely used to infer oceanic and hydrologic processes (e.g., Galewsky et al., 2016), and in paleoceanographic and paleoclimatic studies, such a relationship is used to reconstruct past salinity fields (e.g., Conroy et al., 2017; Risebrobakken et al., 2003; Simon et al., 2020). This relationship stems from the regional atmospheric moisture balance, or evaporation minus precipitation (E-P), which affects both salinity and $\delta^{18}O$ in a similar manner; precipitation leads to freshening and lower $\delta^{18}O$ values, whereas evaporation leads to increased salinity and higher $\delta^{18}O$ values (Craig & Gordon, 1965). This relationship represents the mixing line between a theoretical ocean endmember and a MW endmember. In tropical regions, deviations from this relationships are given by changes in $\delta^{18}O_{MW}$ related to seasonality of precipitation of $\delta^{18}O$ values, changes in moisture source regions, rain re-evaporation, and cloud type and microphysics (Konecky et al., 2019). At high latitudes, seasonal sea ice melt and formation imposes a strong effect on salinity-$\delta^{18}O$ relationships (Bauch et al., 1995, 2005; Rohling, 2013). In the interior ocean $\delta^{18}O$ is considered a conservative water mass tracer (Gebbie & Huybers, 2010; Millet et al., 2024). Although fractionation occurs during biological processes (McConnaughey, 1989), we assume that these are negligible relative to the large scale effect of ocean circulation.

At high-latitudes, $\delta^{18}O$ is a powerful freshwater tracer for two reasons: (a) oxygen-18 in water vapor is progressively depleted as it moves to higher latitudes from its temperate source region. This is known as Rayleigh distillation and results in extremely negative $\delta^{18}O$ at high latitudes (Craig & Gordon, 1965), and thus, it is a sensitive tracer of MW inputs. (b) Sea ice, conversely, has an isotopic composition close to that of the seawater from which is formed, only slightly enriched due to the fractionation between sea ice and seawater (Melling & Moore, 1995). Thus, sea ice melting will reduce salinity but have a comparatively small effect on isotopic composition, whereas brine exclusion during freezing increases seawater salinity with little accompanying change in isotopic composition (Frew et al., 2000). Because of these comparatively different effects one can define a mixing model between the Oceanic (OC), MW, and SIM endmembers and quantify their respective contribution (Frew et al., 2000; Östlund & Hut, 1984). Such a mixing model has been applied in regional studies where the MW endmember isotopic composition can be reasonably assumed to be unique (e.g., Bauch et al., 1995; Hennig et al., 2024; Meredith et al., 2018). To apply this mixing model to the extant global $\delta^{18}O$ measurements it is necessary to constrain $\delta^{18}O_{MW}$ also globally. However, this is not straightforward as $\delta^{18}O_{MW}$ varies not only regionally due to Rayleigh distillation but also depends on the hydrological processes involved (Konecky et al., 2019).

The isotopic composition of MW can be directly measured from precipitation or inferred from the seawater salinity-$\delta^{18}O$ relationship. The Global Network for Isotopes in Precipitation (GNIP; https://www.iaea.org/) provides a database of direct $\delta^{18}O_{MW}$ measurements, however, these are generally sparse (Bowen & Revenaugh, 2003), and even sparser in the ocean, challenging direct applications for oceanographic studies. Adding to this limitation, in some regions the advection of water masses can exert a larger influence on $\delta^{18}O$ in seawater than local precipitation (Meredith et al., 1999), meaning that $\delta^{18}O_{MW}$ measured directly in precipitation may not be accurately represented by the isotopic signature of the water masses in that region. Inferring $\delta^{18}O_{MW}$ from the salinity-$\delta^{18}O$ relationship can account for the effects of advection; however, this approach has its own challenges as the salinity-$\delta^{18}O$ relationship varies among water masses depending on their surface origin. We frame this as a water mass problem: "Where did a given water parcel last interact with the atmosphere through the freshwater cycle?". This water mass problem can be addressed by identifying and tracing water mass properties. We apply an unsupervised machine learning approach, the self-organizing map (SOM), to cluster co-located measurements of ocean salinity, temperature and $\delta^{18}O$ into representative water masses. These clusters are used to estimate $\delta^{18}O_{MW}$

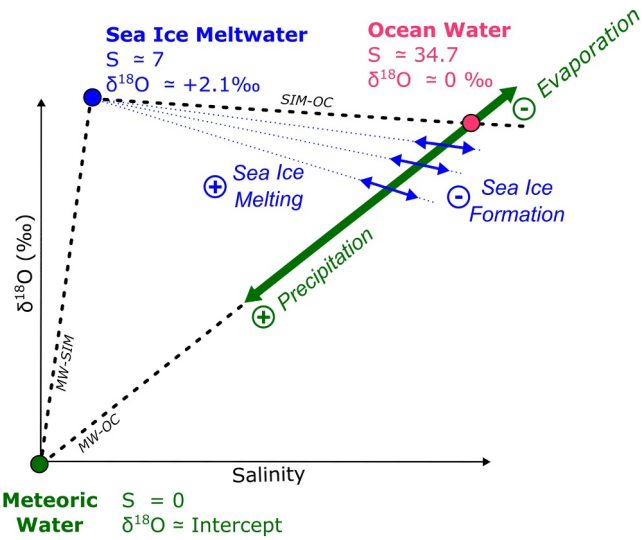

Figure 1. The representation of the three endmember mixing model in salinity-δ^{18}O space for high-latitude water masses. Endmember locations represent 100% contribution of that endmember (and 0% of the other two). Dashed black lines represent the pure mixture of two endmember. The meteoric water (MW) and ocean water (OC) is the dominant relationship in the ocean and is determined by precipitation/evaporation (green arrow) that follows the MW-OC mixing line. In polar regions, addition of sea ice meltwater (SIM) by sea ice melting and removal by sea ice formation create deviations from the MW-OC-only mixing line, represented by dotted blue lines that converge on the SIM endmember. The space inside the triangle defines positive contributions (blue +) relative to the MW-OC mixing line whereas sea ice formation will result in a change in the opposite direction across the MW-OC line and outside of the triangle (blue −). MW is also divided between positive contributions (green +) to freshwater and negative contribution through evaporation (green −) relative to the OC endmember. This division is located at SIM-OC mixing line. The space above the line represents evaporation and below precipitation.

via salinity-δ^{18}O relationships. We then estimate the contribution of MW and SIM and their changes over time in subpolar and polar water masses.

2. Methods

2.1. The Self Organizing Map

A SOM is a competitive neural network based on unsupervised learning. SOMs take in data as a grid of neurons that are spatially adjusted during training, and are typically used for dimensionality reduction and spatial and temporal pattern identification with noisy data (Kohonen, 1982, 2014; Y. Liu et al., 2006). For our specific case, one of the main advantages of SOM to solve the water mass problem at hand is the ability to preserve the topology of the input data while reducing its dimensionality, that is, the relative distance and relationships between the input data are preserved. This increases the interpretability of the output as each cluster represents a different "type" of water mass (Solidoro et al., 2009; Vilibić et al., 2011). Compared to other widely used methods for dimensionality reduction and pattern identification, such as Empirical Orthogonal Function or Principal Component Analysis, SOM offers greater interpretability and pattern extraction (Y. Liu & Weisberg, 2005; Reusch et al., 2005). Here, we use the MATLAB SOM-Toolbox version 2.0 (Kohonen, 2014; Vesanto & Alhoniemi, 2000).

The SOM has two layers, the input layer which consists of the original data, and the output layer of neurons which is organized according to the topology of the data, typically as a 2D map in Euclidean space (Jouini et al., 2016; Vesanto & Alhoniemi, 2000). Our input layer is the existing and available co-located absolute salinity (S_A), conservative temperature (θ) and δ^{18}O measurements taken from the NASA GISS Seawater Oxygen-18 Database (Schmidt et al., 1999), CISE-LOCEAN data sets (Reverdin et al., 2022) and some additional data from the Amundsen Sea (Hennig et al., 2024), and from the West Antarctic Peninsula (available at https://www.bodc.ac.uk). If required, practical salinity and in situ temperature were converted to absolute salinity (hereinafter, S_A) and conservative temperature (θ) according to TEOS-10 (McDougall & Barker, 2011). Each neuron in the output layer is connected to all neurons in the data in the input layer by synaptic weights (an illustrative example of the SOM architecture can be found in Jebri et al., 2022). During the learning process, these weights are updated according to the relations of neighboring neurons. At the end of the training process, the neurons have been organized to represent the topology of the original data in a 3×4 neural rectangular map (a total of 12 neurons), and the neuron that best matches the input is the "winning neuron" also known as the Best Matching Unit (BMU) (J. Liu et al., 2016). Then a cluster is formed with each input data point labeled with the same "winning neuron" and represents a water mass type. Murray et al. (2023) also used the SOM in the context of δ^{18}O in seawater; however, their implementation differs from ours in that they applied the SOM on interpolated δ^{18}O and salinity fields while prescribing a large number of neurons, then they looked at salinity-δ^{18}O relationships over regions of interest that were determined graphically on the resulting BMU field. Here we use the SOM on the raw data to directly identify salinity-δ^{18}O relationships using a much smaller number of neurons.

The map topology is dictated by the training parameters of the SOM, that are user defined, for example, map size, normalization, training type, lattice, and sheet shapes, neighborhood radius and number of training cycles. Our parametrization choice is based on a sensitivity analysis of the identified salinity-δ^{18}O, where the map size and neighborhood radius during the fine training, the second training phase, appeared as the most important parameters. We used a rectangular map, which is the standard topology in literature (López-Rubio & Díaz Ramos, 2014). Our map size (3×4) choice is based on the elbow criterion—that is, the point at which adding neurons reduces topographic error without significantly increasing quantization error, indicating an optimal map size (Figure S1 in Supporting Information S1) (Schumann, 1999). We also found that a larger map reduces the

amount of data per cluster and results in salinity-δ^{18}O relationships that are not representative of the expected mixing line between the ocean and the MW endmembers. The neighborhood radius during the fine training also appeared to be important for the identified salinity-δ^{18}O relationships, where too small radii resulted in an over-representation of local relationships. The rest of the parameters (e.g., type of neighborhood or training length) had a negligible impact of the salinity-δ^{18}O relationships. In general, we found a compromise between the number of data points available, the amount of water mass types, and the relationships among them that resulted in a coherent distribution of clusters according to the prior knowledge of water masses and plausible $\delta^{18}O_{MW}$ values. More details regarding the sensitivity analysis are presented in Supporting Information S1.

2.2. The Three Endmember Mixing Model

Assuming that the properties of the three endmembers in the mixing model are known, it is then possible to estimate their contributions based on tracer conservation equations and mass conservation. A conservative water mass property can be estimated by resolving a system of linear equations where the observed property results from the combination between the fractional contribution of the different endmembers and their properties:

$$S_{SIM} * f_{SIM} + S_{MW} * f_{MW} + S_{OC} * f_{OC} = S_{obs} \quad (1)$$

$$\delta^{18}O_{SIM} * f_{SIM} + \delta^{18}O_{MW} * f_{MW} + \delta^{18}O_{OC} * f_{OC} = \delta^{18}O_{obs} \quad (2)$$

$$f_{SIM} + f_{MW} + f_{OC} = 1 \quad (3)$$

where f_{SIM}, f_{MW} and f_{OC} are the relative fractional contributions of SIM, MW and OC to the observed water parcel admixture. Equations 1 and 2 are the tracer conservation equations that explain the observed salinity (S_{obs}) and oxygen isotopes $\left(\delta^{18}O_{obs}\right)$, respectively, and Equation 3 imposes mass conservation. Note that fractions can be negative, as they represent the relative contributions with respect the different regimes in the salinity-δ^{18}O space (Figure 1).

In salinity-δ^{18}O space, this system of Equations 1–3 is represented as a mixing triangle where sea ice formation and melting processes are manifested as residuals across the MW-OC mixing line that converge into the SIM endmember (blue arrows). Sea ice melting will add freshwater to the water admixture and bring it toward the SIM endmember, whereas sea ice formation removes freshwater from the admixture and produces brine which has the opposite effect and pulls the water admixture away from the SIM endmember (Bauch et al., 1995; Meredith et al., 2018). The MW-OC mixing line defines whether the water admixture contains a positive contribution of SIM through meltwater (blue +) or a negative contribution of SIM through sea ice formation and brine production (blue −). Analogously, MW is divided between positive contributions (green +) to freshwater and negative contribution through evaporation (green −). This division is located at the SIM-OC mixing line. When MW and SIM are negative, OC contributions can be >100%.

This system of Equations 1–3, can be solved by representing them in matrix form. The matrix $\mathbf{A}$ is 3×3 and contains the endmember properties, x is a $3 \times N$ vector containing the mass fractions f for each of the endmembers and b is a $3 \times N$ vector of the observed properties (RHS of Equations 1–3). N is the number of observations in each of the clusters identified by SOM.

$$\mathbf{A}x = b \quad (4)$$

where the solution for x is found by inverting $\mathbf{A}$ and multiplying by the observations $\left(x = \mathbf{A}^{-1}b\right)$.

The endmember properties in $\mathbf{A}$ are unique to each of the 12 clusters, as informed by the SOM (Section 2.2). We estimate the isotopic composition of the MW endmember as the δ^{18}O value at $S_A = 0$ intercept (Fairbanks, 1982; Hennig et al., 2024; Jenkins, 1999). By clustering water mass types according to conservative water mass properties, we are effectively tracing their origin at the surface, which determines the $\delta^{18}O_{MW}$ to which they were exposed when they were formed. Hence, each of the clusters distils the $\delta^{18}O_{MW}$ via different slopes in salinity-δ^{18}O which results in 12 different mixing models with unique $\delta^{18}O_{MW}$ and geometry (Figure 2). In turns, the OC endmember is taken from the other side of the MW-OC mixing line, defined as $S_A = 34.7$, the average deep

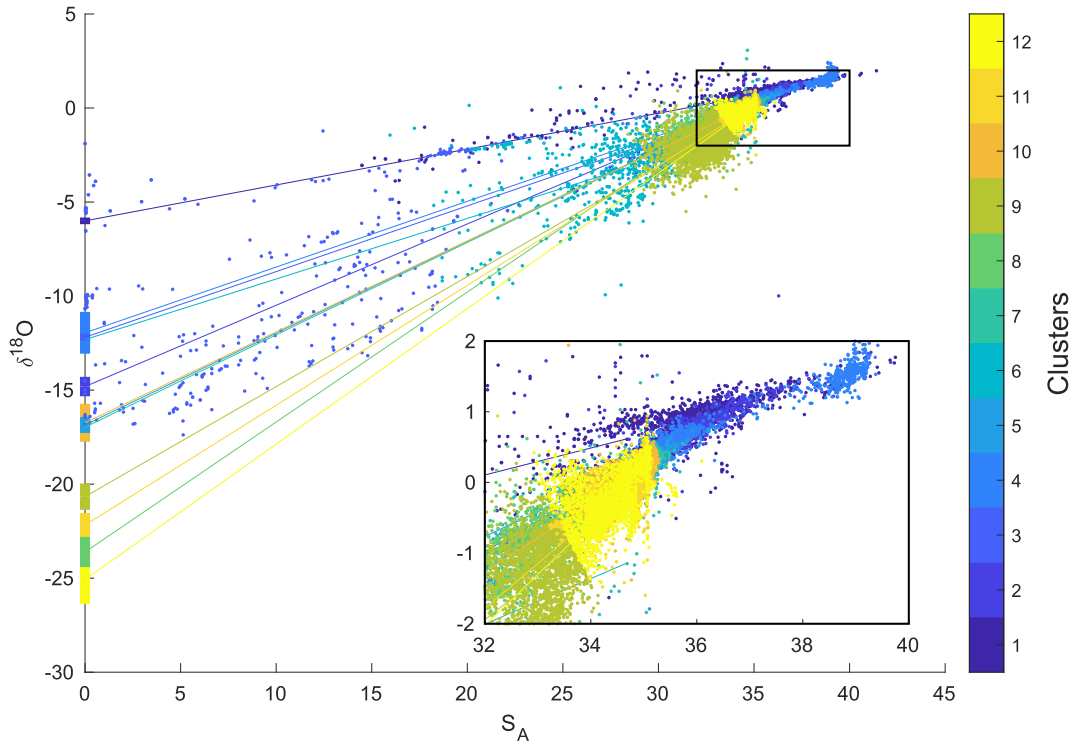

Figure 2. Salinity and $\delta^{18}O_{obs}$ relations for each of the 12 different clusters that define 1 different mixing models with unique geometry. Clusters labeled with high values are typically located in polar regions while those labeled low are in the tropics. The $S_A = 0$ intercept infers the meteoric water isotopic concentration. Vertical bars at $S_A = 0$ indicate the uncertainty by bootstrapping the SOM after adding noise to simulate observations to be "polluted" by sea ice processes.

ocean salinity, and $\delta^{18}O_{OC}$ at the $S_A = 34.7$ intercept. The SIM endmembers properties are defined at $S_A = 7$ and $\delta^{18}O_{SIM} = \delta^{18}O_{OC} + 2.1$ to account for fractionation during sea ice formation, following previous studies in the Southern Ocean (Hennig et al., 2024; Meredith et al., 2008) and the Arctic (Bauch et al., 1995). Although most of studies that employ the mixing model define the oceanic endmember as the prevalent water mass in the region, this is challenging to do so at large scales. The choice of the oceanic endmember representing the interior ocean is motivated by the fact that salinity and $\delta^{18}O$ are largely only modified at surface; Mixing processes in the ocean interior tend to homogenize water mass properties, whereas surface processes such as warming, precipitation or sea-ice formation tend to add structure to the $\theta - S_A$ or salinity-$\delta^{18}O$ curve. Thus we look at the effect of these surface processes relative to average (or representative) interior properties.

The estimates of MW and SIM fractional contributions to the freshwater admixture are sensitive to the definition of the endmembers. The major uncertainty in this analysis is the definition of $\delta^{18}O_{MW}$ via extrapolation of salinity-$\delta^{18}O$ relationship due to two major inherent assumptions. One assumption is (a) that the endmember can be represented by a single discrete value, even when considering different clusters. In reality, one can expect a continuous spectrum of values on every temporal and spatial scale that accounts for variability in the endmembers. In this context, the inferred $\delta^{18}O_{MW}$ inferred here should be taken as an average endmember that can explain the observed $\delta^{18}O$ in seawater across the salinity gradient of a given water mass type. The other key consideration is (b) that the effect of sea ice processes that "pull up/down" the salinity-$\delta^{18}O$ relationships at high latitudes. Although the seasonal formation and melting of sea ice have symmetrically opposite effects in salinity-$\delta^{18}O$ space, they also have opposite effects in the density structure of the water column. Sea ice meltwater stabilizes the water column, whereas the brine excreted during sea ice formation destabilizes it. In our case, sea ice meltwater and brine will rarely cancel each other out when inferring $\delta^{18}O_{MW}$, unless they are present in the same cluster. Hennig et al. (2024) showed clear deviations of the mixing line in the data points at surface (<200 m) that were assumed to be due to the addition of sea ice meltwater and were removed when inferring $\delta^{18}O_{MW}$. Here, we test the sensitivity of the $\delta^{18}O_{MW}$ with respect to sea ice processes and, more in general, the effect of variability

across the MW-OC mixing line. We "polluted" the surface (<200 m) data points with noise and bootstrap the SOM, then recompute the $\delta^{18}O_{MW}$ as the $S_A = 0$ intercept for each of the resulting clusters in the bootstrapping. Specifically, the noise is added to surface data points and increases proportionally with the distance away from the ocean endmember ($S_A = 34.7$; $\delta^{18}O = 0$). We add ±200% of the distance to the ocean endmember to 50% of the surface data (<200 m) for 20 repetitions. In addition, we assume that both $\delta^{18}O$ and salinity contain errors, and thus we use the Total Least Squares method through a Singular Value Decomposition to perform the regression throughout the analysis. The resulting uncertainty ranges from 0.18‰ to 1.29‰ (vertical bars in Figure 2) and is generally larger in the high-latitude clusters and in cluster 4 which is related to river runoff.

To estimate the uncertainty in the contributions of SIM and MW originating from the uncertainty in the endmember properties, we first calculate the sensitivity of those mass fractions in x to the endmember properties in $\mathbf{A}$. Because of the matrix configuration of this linear system, this can be done in a single operation as the partial derivative of x with respect to $\mathbf{A}$. This is also the adjoint of Equation 4, and is resolved as the Kronecker product between the transpose of x and $\mathbf{A}$, resulting in the sensitivity matrix $\mathbf{S}$ (the step-by-step differentiation of Equation 4 is shown in Appendix A):

$$\mathbf{S} = \frac{dx}{d\mathbf{A}} = -x^T \otimes \mathbf{A}^{-1} \tag{5}$$

where $\otimes$ denotes the Kronecker product and $\mathbf{S}$ is the resulting sensitivity matrix of size 3×9 that contains the sensitivity for each calculated endmember fraction f in x with respect each parameter (S_A, $\delta^{18}O$ and mass) of each endmember (MW, SIM, and OC) in $\mathbf{A}$. Then, the uncertainty of the endmember properties either from literature or the bootstraping are used to scale the sensitivities in $\mathbf{S}$. Overall, the resulting uncertainties are an order of magnitude lower than the estimated endmember fraction. These are further discussed in Section 4.2.

3. Results

3.1. Global Distribution of $\delta^{18}O_{MW}$

The distribution of the clusters generated by the SOM are consistent with the current knowledge of water mass distribution (Figure 3). At the surface (<200 m), the tropical regions, the subpolar regions, and the polar regions are clustered together (Figure 3a). The Atlantic inflow into the subpolar North Atlantic is also distinguished by clusters that fall close to the tropical clusters in the eastern side versus the western side. Similarly, the transition from Antarctic Intermediate waters (AAIWs) to subtropical mode waters is also observed. In polar regions, there is more variability in the distribution of clusters, likely due to the regional effects of MW. At greater depths, the polar clusters are found at lower latitudes, consistent with the circulation of high-latitude deep and intermediate waters (Figures 3b–3d). Unfortunately the amount and spatial coverage of available observations below the surface is limited. An additional feature identified by the SOM are regions of river runoff, for example, the Arctic rivers, that are also clustered together (Figure 3a).

The $\delta^{18}O_{MW}$ derived from seawater $\delta^{18}O$ measurements by the SOM shows the expected poleward depletion from Rayleigh distillation, that is, the poleward transport of moisture and its ongoing depletion in heavy isotopes. Our estimates range from about −25‰ in Antarctica to −5‰ in the tropics (Figure 4). This range is similar to the −19.95‰ to −0.79‰ reported by Murray et al. (2023). Although the poleward depletion showed in the $\delta^{18}O_{MW}$ inferred by the SOM fits well with the direct estimates of $\delta^{18}O$ measured directly in precipitation from Global Network of Isotopes in Precipitation (GNIP) (Figures 4a and 5a), there are apparent differences when comparing SOM-inferred $\delta^{18}O_{MW}$ and GNIP at the same locations. Overall, SOM $\delta^{18}O_{MW}$ is lighter than that from GNIP, with increasing disagreement polewards. Such differences have been regionally identified before, and arise from the inherently different nature of GNIP measurements as the true measure of $\delta^{18}O$ in precipitation, and the SOM estimates inferred from salinity-$\delta^{18}O$ which can be strongly affected by ocean circulation. Meredith et al. (1999) showed that in the South Atlantic (at WOCE A11; 45°S) $\delta^{18}O_{MW}$ derived from salinity-$\delta^{18}O$ is also isotopically much lighter (more depleted) than the local precipitation, even accounting for the large error in the salinity-$\delta^{18}O$ extrapolation. They attributed such a difference to the advection of polar waters (Antarctic Surface Waters) at

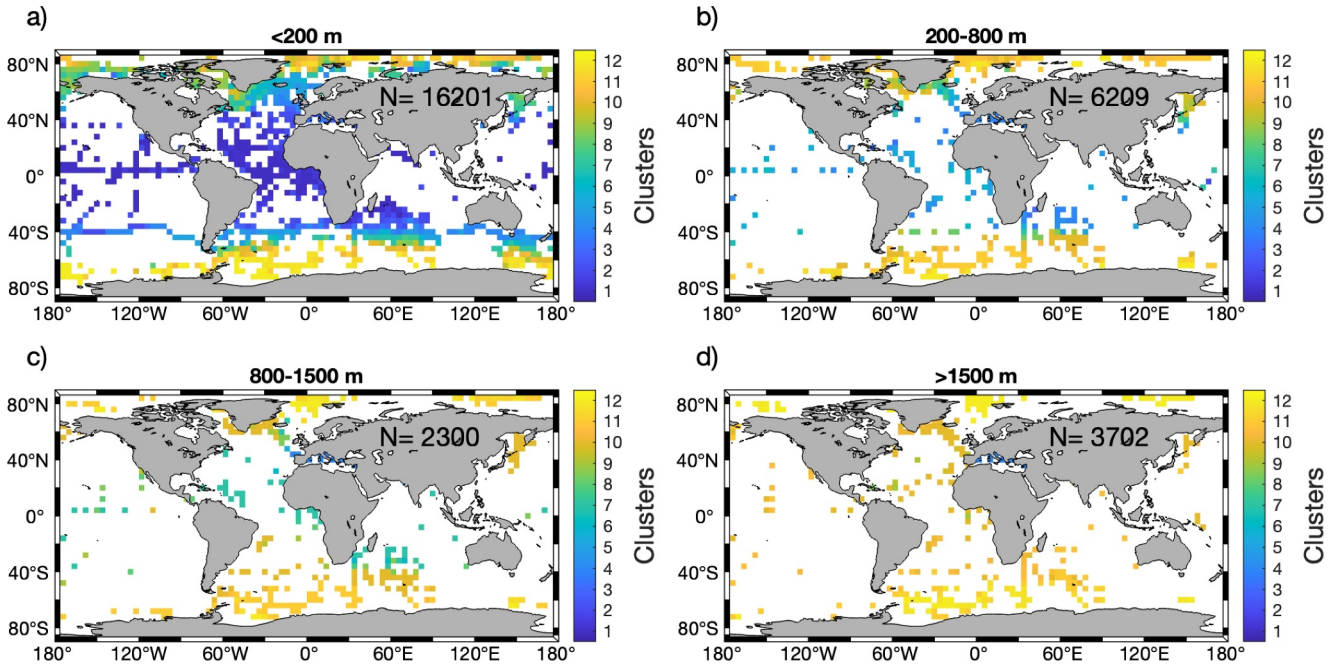

Figure 3. Spatial distribution of each of the 12 different clusters. The values have been regridded and averaged to a 4° × 4° grid for visualization and over depth intervals: surface values above 200 m (a), 200–800 m (b), 800–1,500 m (c) and below 1,500 m (d). N indicates the number of observations in each depth interval.

surface being exposed to the atmosphere further south than their current location, and thus isotopically lighter precipitation. This is evidence of the dominance of advection over local processes in determining the salinity-δ^{18}O relationships (Meredith et al., 1999).

The equatorwards advection of polar waters can explain a large part of the disagreement between SOM and GNIP, especially in those regions subjected to Ekman transport (poleward of ∼30°N and ∼30°S; Wang & Huang, 2004). However, advection alone cannot explain the systematically negative offset in the SOM in tropical regions (∼20°N–20°S), as the opposite effect (and thus positive offset) is expected in waters advected polewards. Vertical mixing is the other obvious candidate that can explain the systematic negative offset. The surface waters mix with those directly beneath, which are typically formed at higher latitudes, and therefore carry a lighter $\delta^{18}O_{MW}$ signal (Figures 4b–4d). Although constraining the mechanisms behind the systematic lighter $\delta^{18}O_{MW}$ estimated here with respect to GNIP is beyond the scope of this study, from our results we conjecture that the effects of advection and mixing with water formed at higher latitudes result in the systematic offset in the SOM compared to GNIP. This indicates that the combined effect of advection and vertical mixing may exert a greater effect in the freshwater budget versus local precipitation in the surface global ocean. We also note that there is substantial variability in GNIP (gray lines in Figure 5b), whereas SOM represents the ocean with just a few clusters, in addition to most of the overlapping GNIP data being collected in tropical islands and not directly over the ocean, which may introduce additional biases. The only place where SOM infers a more positive (enriched) $\delta^{18}O_{MW}$ is in the Arctic (>70°N), where multiple rivers discharge, together with glacier melt and precipitation, results in $\delta^{18}O_{MW}$ values that range from approximately −10‰ to −25‰ (Kopec et al., 2024). This highly complex hydrological environment presents challenges for our SOM-based approach, which necessarily averages over these diverse inputs.

Overall, the influence of advection and vertical mixing on salinity-δ^{18}O relationships and the mismatch with δ^{18}O measured directly in precipitation has important consequences for studies that rely on the assumption of a known $\delta^{18}O_{MW}$ and assumed salinity-δ^{18}O relationships, such as the present study but also paleosalinity reconstructions of sediment cores (Rohling & Bigg, 1998). Regarding the present study, and in the context of the mixing model to determine the MW and SIM contributions (Figure 1), the $\delta^{18}O_{MW}$ inferred here also falls close to that used by previous regional studies using a mixing model to estimate MW and SIM, for example, Meredith et al. (2008)

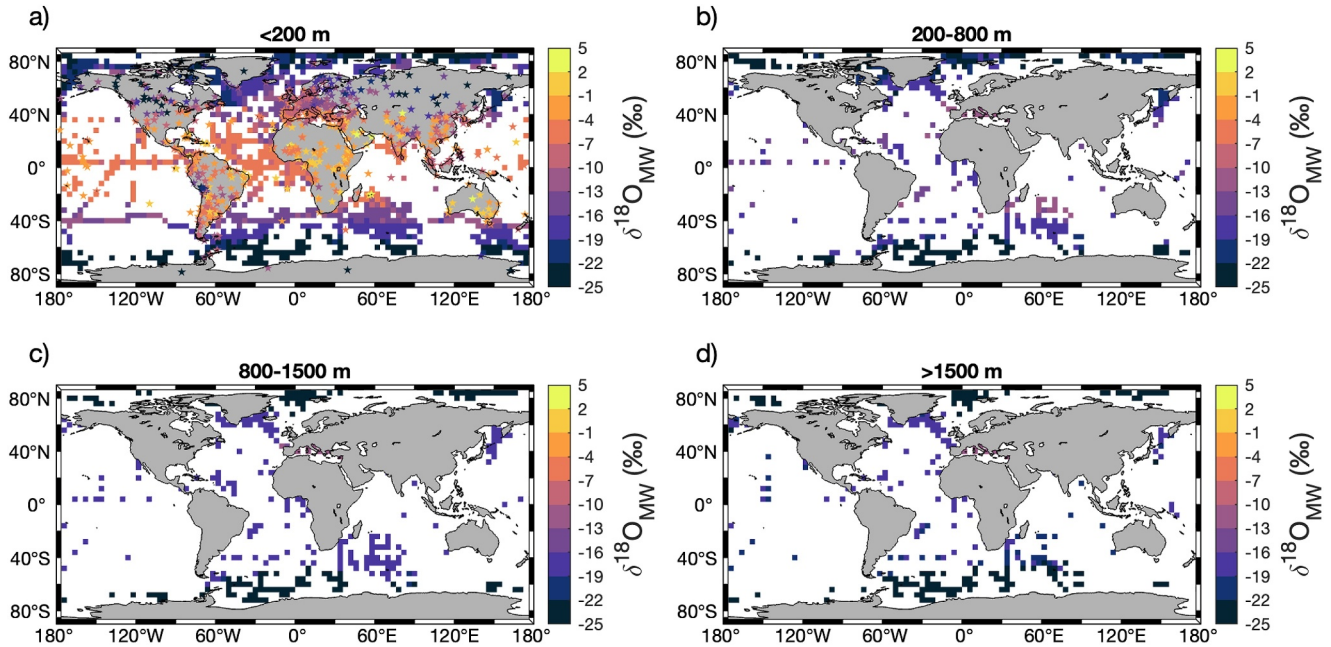

Figure 4. Spatial distribution of the isotopic concentration in meteoric water inferred from the self-organizing map (SOM) at different depth intervals: surface values above 200 m (a), 200–800 m (b), 800–1,500 m (c) and below 1,500 m (d). Surface estimates from the SOM (gridded estimates) are compared to direct observations of δ^{18}O in precipitation in from the Global Network of Isotopes in Precipitation shown as stars (a). The values estimated by the SOM have been regridded and averaged to a $4° \times 4°$ grid for visualization and over the described depth intervals.

used $\delta^{18}O_{MW} = -17‰$ in the West Antarctic Peninsula, Hennig et al. (2024) $-30‰$ in West Antarctica, and Bauch et al. (1995) $-21‰$ for the Arctic river runoff.

The residuals of δ^{18}O from the MW-OC mixing line give a sense of the processes that affect the estimates of $\delta^{18}O_{MW}$. These are relatively small in the tropical and subtropical regions (mostly clusters 1–5) and is likely associated to changes in $\delta^{18}O_{MW}$ through variability in the MW endmember such as El Niño-Southern Oscillation (Conroy et al., 2017; Murray et al., 2023), although secondary water masses that are misrepresented in the sampling might also result in some of the residuals (Benway & Mix, 2004). The latter is the case for the large positive residuals (>5‰) at the equator, which are associated with the Amazon river. At higher latitudes (mostly clusters 6–12) residuals get larger, especially in the northern hemisphere. Here, the very negative values around 70°N are associated with the Arctic rivers. At these latitudes, where sea ice processes are expected, it becomes more challenging to attribute the residuals to a secondary water mass or sea ice processes that could also potentially bias the definition of the MW-OC mixing line (Section 2.2). Here, we assume that for cluster 6–12, the variability across the MW-OC mixing line results from sea ice processes according to Figure 1, and we estimate the contributions of MW and SIM to the sampled water admixture (Sections 3.2 and 3.3). We also quantify the sensitivity of these contributions with respect to the definition of the endmember and discuss the implications for the estimated MW and SIM contributions (Section 4.2).

3.2. Spatial Patterns of Meteoric Water and Sea Ice Meltwater

Overall, contributions to the ocean freshwater content at high latitudes are dominated by MW over SIM (Figure 6). Positive MW contributions indicate an addition of freshwater by precipitation to the water column, whereas negative values refer to the removal of freshwater through evaporation. Analogously, positive SIM indicates the freshwater added into the ocean by sea ice melting, whereas negative values indicate the equivalent freshwater content that has been removed by sea ice formation and brine production (Bauch et al., 1995; Hennig et al., 2024; Meredith et al., 2018).

In the Arctic surface layer (<200 m), the runoff from the major Arctic rivers contribute to maintaining the halocline in the Kara (77°N; 77°E) and Laptev Sea (76°N; 125°E), as well as in the Beaufort Sea (72°N; 137°W). In the northeast of Greenland, high MW fractions are also detected, and may be explained by a combination of the

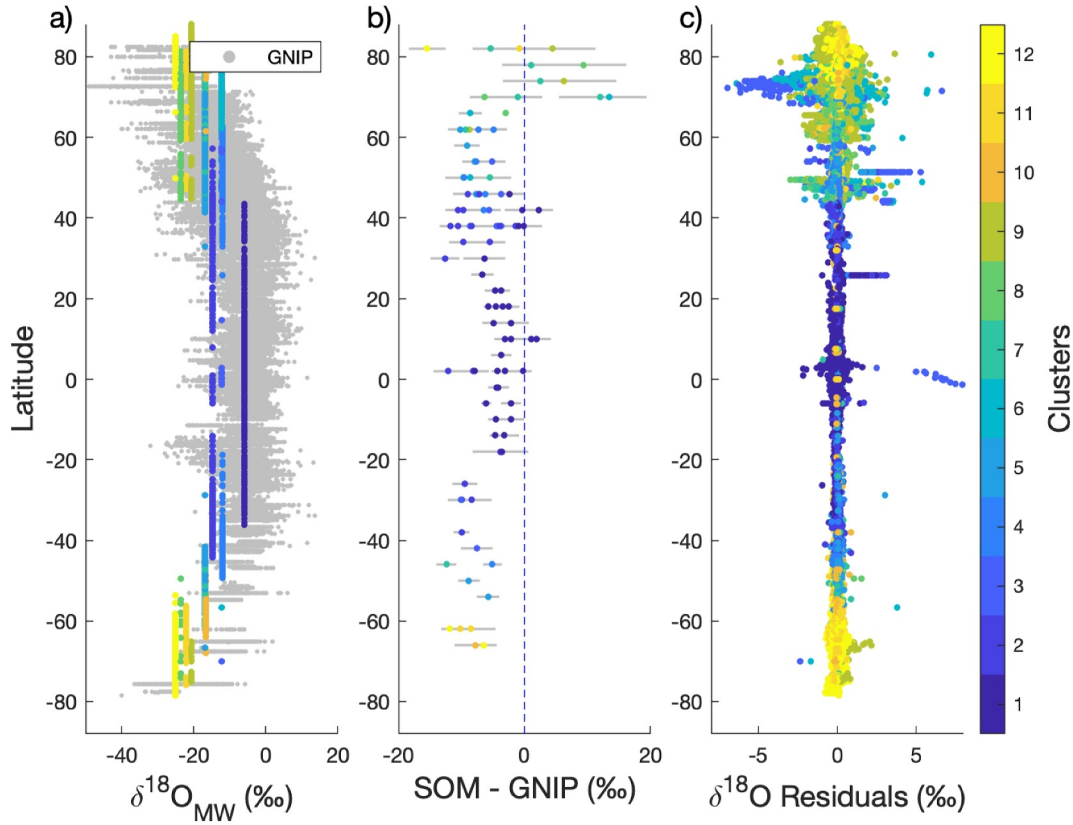

Figure 5. Latitudinal comparison of the shallowest 20 m from the self-organizing map and all available observations in precipitation from Global Network of Isotopes in Precipitation (a) and their difference of the spatially co-located values after regridding and averaging on a 4° × 4° grid (b). The $\delta^{18}O$ residuals from the meteoric water-ocean water (MW-OC) mixing line indicate the variability across the dominant MW endmember (c).

sustained melting of the northeast Greenland Ice Sheet (Khan et al., 2014) and river runoff crossing the Arctic and exiting via this route (Granskog et al., 2012). These contribute to large amounts of MW to the surface Arctic. SIM, contributing to a lesser extent, follows roughly the sea ice edge, especially in the Barents Sea and the Beaufort Sea where SIM contributes with <10% of the halocline waters (Figure 6b). The imprint of sea ice formation and export is shown in the Kara and Laptev Sea, as well as in the Beaufort Sea and at Canadian Archipelago (Baffin and Hudson Bay) where very negative SIM values are indicative of significant amounts of freshwater being removed from the ocean and brine being produced. Sea ice formation is also present, but at lesser extent, in the north-east of Greenland. These locations agree well with our knowledge on the distribution of open polynyas in the Arctic where sea ice formed and subsequently exported (Cornish et al., 2022; Tamura & Ohshima, 2011). Although brine is denser than the surrounding seawater and sinks, there are only few deep observations available at these sit, mostly in the Labrador Sea and Hudson Bay (Figures 6d, 6f, and 6h). At deeper levels (>200 m), below the Arctic halocline, a negative contribution of MW represents the inflow of saltier Atlantic waters (Sverdrup, 1950) that have been subjected to evaporation upstream. At these depths, SIM is also present, most likely after entraining the Atlantic inflow waters and slightly compensating the effect of evaporation (in terms of salinity).

In the Southern Ocean, MW dominates over SIM at surface (<200 m). Around 40–60°S MW comes most likely from direct meteorological precipitation. Closer to Antarctica precipitation decreases (Boisvert et al., 2020) and contributions from drifting icebergs may also contribute to observed MW concentration (Merino et al., 2016). Sea ice meltwater contributions are also much smaller here, and are most prominent around the Ross Sea. At greater depths (200–1,500 m; Figures 6c and 6e), the MW pattern becomes more heterogeneous, which may suggest a more localized source rather than precipitation, such as basal melting. High fractions of MW are found in the Amundsen Sea and Weddell Sea, coinciding with previous studies (Brown et al., 2014; Hennig et al., 2024). Such high fractions are expected as tributary glaciers discharge freshwater in these regions (Rignot et al., 2011).

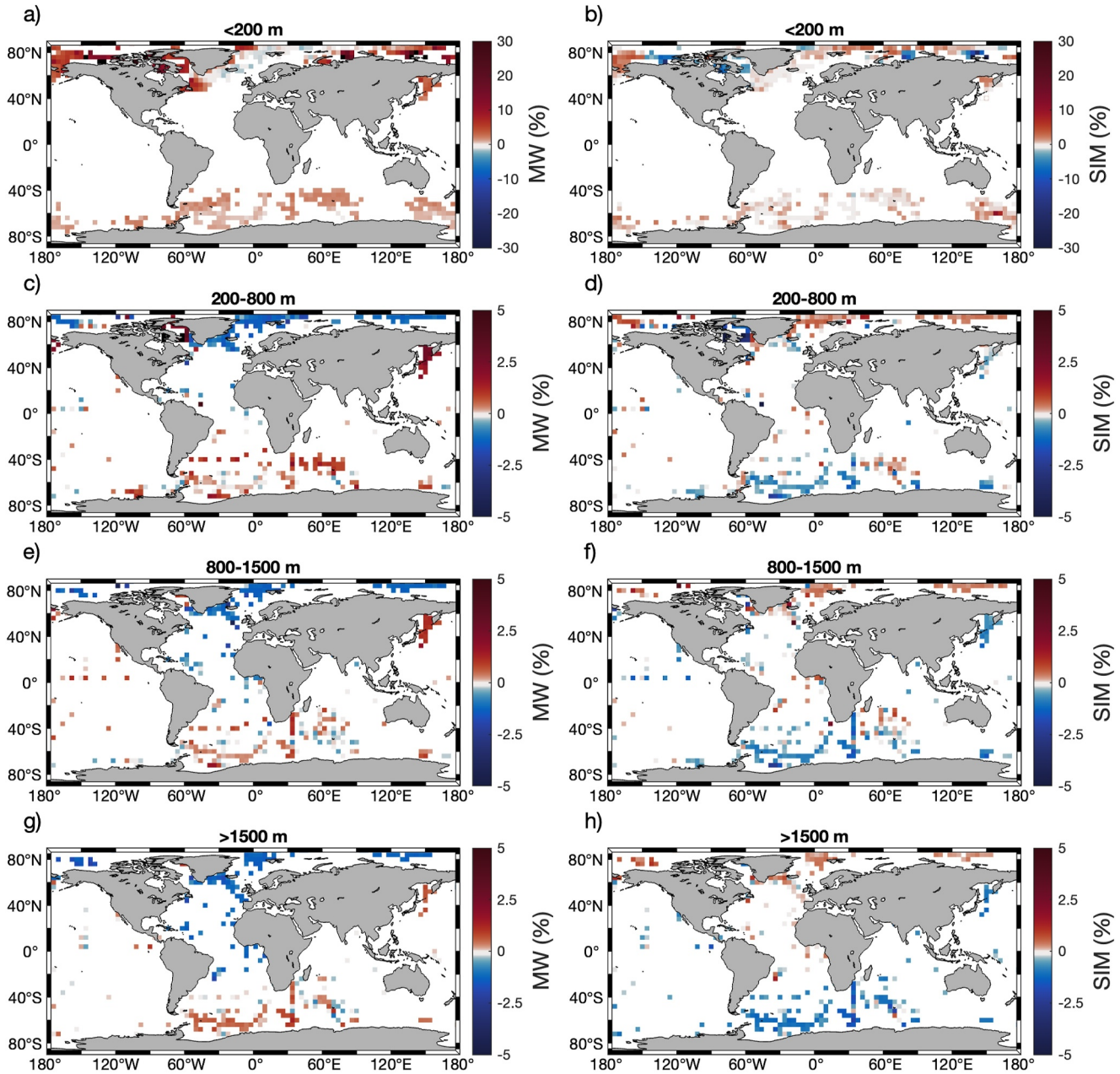

Figure 6. Spatial distribution of meteoric water (MW) and sea ice meltwater (SIM) contributions to the seawater admixture computed from the mixing model, in percentages. Left column for MW, and right for SIM. The values have been regridded and averaged to a 4° × 4° grid for visualization and over the described depth intervals. Note that the colorscale for depths ≥200 m (c–h) is a smaller order of magnitude than that for the surface plots (<200 m; a–b).

However, we note that precipitation and glacial melt cannot be distinguished solely from $\delta^{18}O$. At these depths the imprints of brine production through sea ice formation become present. The vertical asymmetry in SIM in the Southern Ocean results from the opposing effects that sea ice melting and formation have in the water column. Sea ice melting stabilizes the water column and therefore anomalies are likely to be constrained near the surface, whereas sea ice production destabilizes the water column as brine abandons the surface. This differential effect is further enhanced by the seasonal aliasing in the observations, as these measurements were collected during summer. At even greater depths (>1,500 m; Figures 6g and 6h), the large circulation pattern emerges with the spreading of Antarctic waters northwards into the subtropics, carrying a MW freshening and brine signal as far north as the subtropics (>1,500 m).

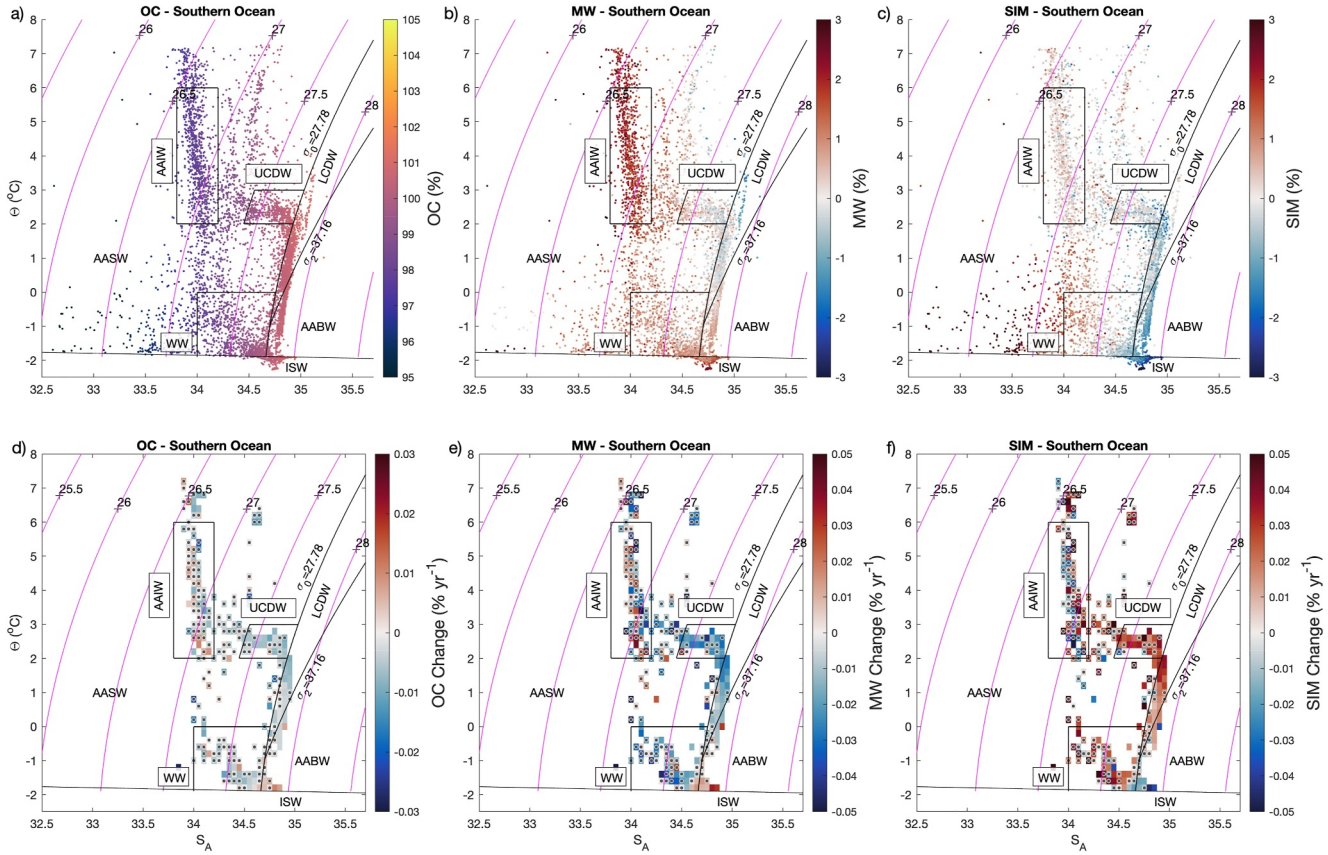

Figure 7. Contributions of the ocean water, meteoric water and sea ice meltwater endmembers averaged per major water mass in the Southern Ocean. Relative contributions are shown in θ-S space (a–c) where definition of the water masses follow those in Table 1, with corresponding trends for the endmember contributions over the 1980–2023 period (d–f). For a trend to be detected, the observed period must cover at least 5 years with observations taken during at least three different years over the 1980–2023 period. Dots indicate non-significant trends. The water masses are: ice shelf water (ISW), Antarctic bottom water (AABW), lower circumpolar deep water (LCDW), upper circumpolar deep water (UCDW), winter water (WW), and Antarctic intermediate water (AAIW).

3.3. Quantifying the Role of Meteoric Water and Sea Ice Meltwater in Water Mass Transformation and Changes

When the distribution of MW and SIM is displayed in $\theta - S_A$ space, clear patterns of the influence of these freshwater sources in the water mass distribution emerge (Figures 7 and 8). As expected, the OC contribution increases with increasing salinity and is 100% where the OC endmember is located ($S_A = 34.7$ and corresponding δ^{18}O) and beyond 100% in regions where MW and SIM are negative. Although MW shows, to a great extent, the opposite pattern to OC (high MW contributions at low salinities and vice-versa), there are nuances to its distribution that relate to the necessary mass exchanges between endmembers to form and transform water masses. The definitions of the water masses and their mean properties in terms of $\delta^{18}O_{MW}$ and endmember contributions are detailed in Tables 1 and 2, respectively.

3.3.1. Southern Ocean

Antarctic bottom water (AABW) is tightly linked to sea ice formation as suggested by its brine content (Figure 7). Initially, Antarctic surface waters (AASW) freeze, leading to sea ice formation and brine rejection, transforming AASW into winter water (WW; Figure 7c). The posterior mixing of WW with the underlying lower circumpolar deep water (LCDW), produces high salinity shelf water (HSSW). In some locations (e.g., Ross and Weddell Seas, Prydz Bay), HSSW flows into the ice shelf cavity, inducing basal melting, which makes HSSW to become fresh and supercool (below the freezing point), becoming ice shelf water (ISW) (Silvano et al., 2023). The signatures of brine and basal melt in ISW are clearly seen in the estimates of both MW and SIM (Figures 7b and 7c). Once formed, a fraction of ISW/HHSW escapes the cavity, where it mixes with the surrounding LCDW, and is

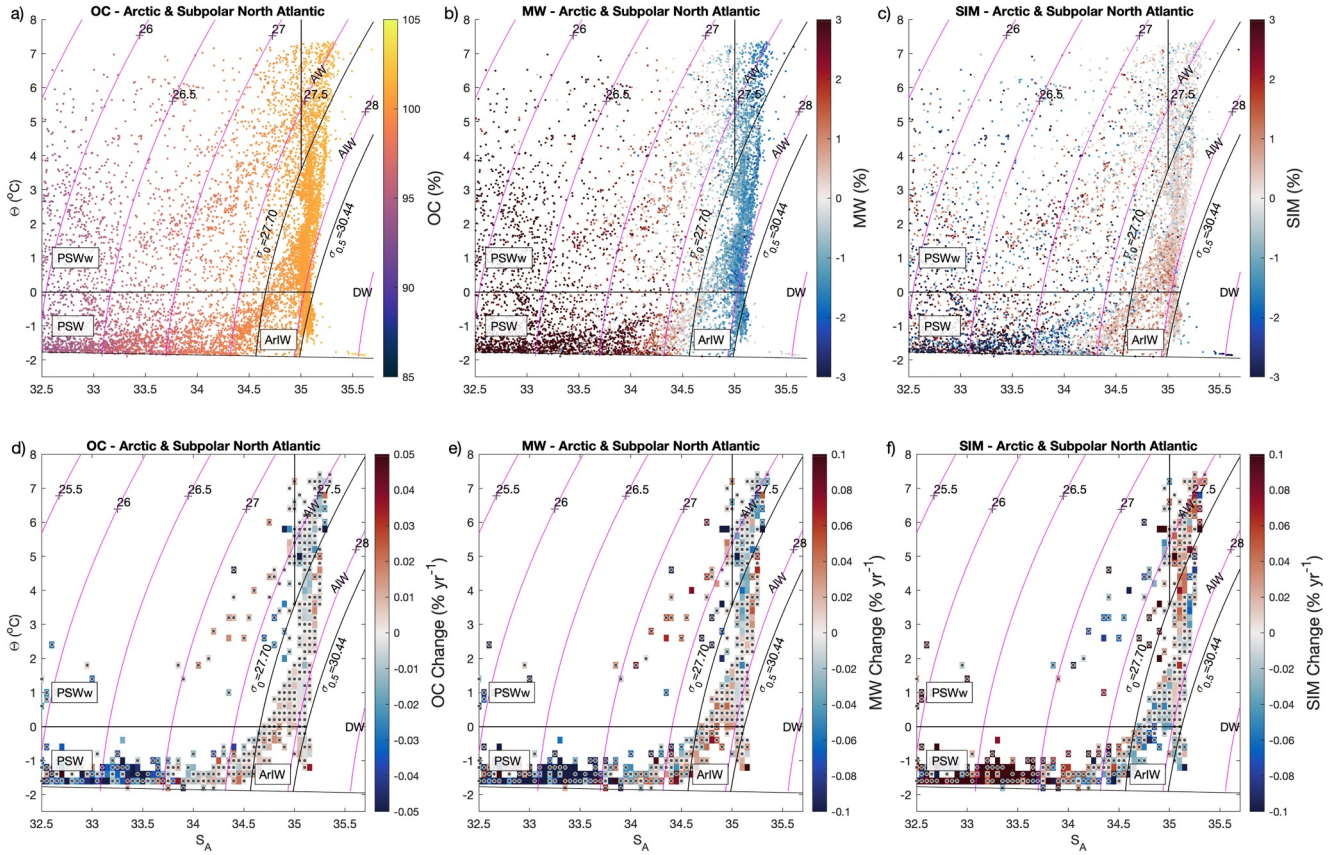

Figure 8. Same as Figure 7 but for the Arctic and Subpolar North Atlantic. The water masses are: deep water (DW), Arctic origin intermediate water (ArIW), Atlantic origin intermediate water (AIW), Atlantic water (AW), polar surface water (PSW), and warm PSW (PSWw). The definition of these water masses can be found in Table 1.

transformed into AABW (Figures 7b and 7c) (Nicholls et al., 2009; Silvano et al., 2023). AABW preserves some of the MW and SIM content, where the loss in glacial meltwater is larger than the loss of brine, resulting in the slight salinity increase observed in $\theta - S_A$ space (Figure 7). The strong anticorrelation of MW and SIM in $\theta - S_A$ space is partially given by the mass balance between all endmembers (Equation 3), but also results from the

Table 1
Definition of Water Masses According to Density, Conservative Temperature, and Absolute Salinity

	Water Mass	σ_0	$\sigma_{0.5}$	σ_2	θ (°C)	S_A (g kg^{-1})
Southern Ocean	Ice shelf water (ISW)				<−1.9[a]	
	Antarctic bottom water (AABW)	>27.78[b]		>37.16[b]	>−1.9	
	Lower circumpolar deep water (LCDW)	>27.78[b]		<34.75[b]		
	Upper circumpolar deep water (UCDW)	27.4–27.78[b]			>2 and <3	
	Antarctic intermediate water (AAIW)				>2 and <6	>33.8 and <34.2[c]
	Winter water (WW)	<27.78[b]			<0.5	>34
Arctic and Subpolar North Atlantic	Deep water (DW)		>30.44[d]			
	Arctic origin intermediate water (ArIW)	>2.7[d]	<30.44[d]		<0[d]	
	Atlantic origin intermediate water (AIW)	>27.7[d]	<30.44[d]		>0[d]	<35.5
	Polar surface water (PSW)	<27.7[d]			<0[d]	
	Atlantic water (AW)	<27.7[d]				>35[d]

Note. All constraints must be satisfied for each data point to be classified as the corresponding water mass. [a]Carmack and Foster (1977). [b]Orsi et al. (1995). [c]Xia et al. (2022). [d]Rudels et al. (2005).

Table 2
Average Water Mass $\delta^{18}O_{MW}$ Inferred From the Self-Organizing Map and the Associated Uncertainty Estimated by the Bootstrapping, As Well As Average Ocean Water (OC), Meteoric Water (MW), and Sea Ice Meltwater (SIM) Contributions Estimated Through the Three-Endmember Mixing Model

	Water Mass	$\delta^{18}O_{MW}$	OC (%)	MW (%)	SIM (%)
Southern Ocean	Ice shelf water (ISW)	−25.1 ± 1.3	100.5	1.3	−1.9
	Antarctic bottom water (AABW)	−24.3 ± 1.1	100.6	0.5	−1.1
	Lower circumpolar deep water (LCDW)	−21.5 ± 0.7	100.7	0.0	−0.6
	Upper circumpolar deep water (UCDW)	−16.7 ± 1.0	100.2	0.1	−0.3
	Antarctic intermediate water (AAIW)	−16.9 ± 0.7	97.9	1.9	0.2
	Winter water (WW)	−24.9 ± 1.3	99.2	1.2	−0.3
Arctic and Subpolar North Atlantic	Deep water (DW)	−25.1 ± 1.3	101.1	−1.3	0.3
	Arctic origin intermediate water (ArIW)	−24.6 ± 1.2	100.7	−1.3	0.5
	Atlantic origin intermediate water (AIW)	−18.2 ± 0.9	100.1	−1.2	0.22
	Polar surface water (PSW)	−21.8 ± 0.9	94.9	5.1	0.02
	Atlantic water (AW)	−16.5 ± 0.4	101.3	−1.2	−0.1

mechanistic response of sea ice formation to freshening. Glacial freshwater release increases surface stratification and inhibits convection which enhances sea ice formation (Marsland & Wolff, 2001; Merino et al., 2018).

In recent decades, AABW has warmed and freshened, and consequently, its formation (Li et al., 2023) and its export have reduced (Zhou et al., 2023). To estimate changes in the freshwater budget of these water masses, we regrid OC, MW, and SIM estimates in $\theta - S_A$ space and calculate the trends for each of the $\theta - S_A$ bins (Figures 7d–7f). For a trend to be detected, the observed period must cover at least 5 years with observations taken during at least 3 different years. Statistically significant trends are given by p-value<0.05. Although these trends do not necessarily cover the same period, and some are not significant, they are relatively coherent in $\theta - S_A$ space (Figures 7d–7f). During the period 1980–2023, the SIM trend in AABW is in the direction of becoming less negative, that is, a reduction in the net amount of sea ice formation in the waters that contribute to the AABW. This gain in sea ice melt (positive SIM trend) is partially balanced by a decrease in meteoric water (negative MW trend). Such change is coherent along the mixing line with the upper and lower CDW and agrees with previous literature that attributed the freshening of AABW to reduction of sea ice formation (Haumann et al., 2016; Zhou et al., 2023). Although trends in AAIW are overall not significant, they suggest less SIM (negative SIM trends) and more MW. Such change may arise via reduce formation and transport of sea ice (Haumann et al., 2016) that was indicated by trends in AABW. Surprisingly, ISW shows an opposite trend and indicates a significant increase in sea ice formation (negative SIM trend) and an increase in MW, likely due to glacial melt, even if ISW and AABW formation are linked. These changes are also visible as salinity trends (AABW getting fresher and ISW saltier), however, with much fewer significant trends and less coherent in $\theta - S_A$ space. The coherence and significance in endmember trends is given by trends in $\delta^{18}O$ (Figure S2 in Supporting Information S1). Kim and Timmermann (2024) showed that $\delta^{18}O$ has a higher signal-to-noise ratio compared to salinity, and therefore anthropogenic signals emerge decades earlier, which might be the reason why changes in $\delta^{18}O$ and, by extension SIM and MW, are more coherent than changes in salinity.

3.3.2. Arctic and Subpolar North Atlantic

In contrast to the Southern Ocean, dense waters in the Subpolar North Atlantic are formed primarily via buoyancy loss to the atmosphere (e.g., Bosse et al., 2018; Våge et al., 2015) with little exchange with the other freshwater reservoirs (Figure 8). The evaporative signal (negative MW) of the Atlantic water (AW) can be traced for the entire transformation line into Arctic-origin intermediate water (ArIW), and further into the deep water (DW). In the Arctic, polar surface water (PSW; Rudels et al., 2005) occupies the halocline, which shows the highest MW content that is attributed to the Arctic rivers. PSW also shows a large content of brine resulting from sea ice formation (negative SIM) in the Arctic polynyas (Figures 6a and 6ure 8c).

The Subpolar North Atlantic experienced anomalous freshening during the 1970–1990s, primarily linked to the freshening of the Atlantic inflow. After the 1990s, this trend reversed (Glessmer et al., 2014). Much of the earlier

freshening has been attributed to the Great Salinity Anomalies (Dickson et al., 1988; Holliday et al., 2008), though the origin of these anomalies—whether from Arctic or Atlantic sources, and whether driven by sea ice or precipitation—remains a subject of ongoing debate (e.g., Allan & Allan, 2024; Belkin, 2004; Boyer et al., 2007; Mysak et al., 1990; Sundby & Drinkwater, 2007). To our knowledge, $\delta^{18}O$ has not previously been applied to trace the sources contributing to the transition from the fresher 1970–1990s period to the more saline conditions that followed. Although few statistically significant trends are observed in SIM and MW contributions in Arctic and Subpolar North Atlantic water masses over the 1980–2023 period, the changes are relatively coherent across adjacent θ-S bins. These patterns still provide qualitative insights into broader shifts. The clearest signal is an increase in SIM in the less dense PSW relative to MW and OC, possibly indicating a shift toward less sea ice. In contrast, ArIW shows reduced SIM relative to MW and OC. Taken together, these trends may reflect a net decline in sea ice, potentially leading to decreased SIM input into the ArIW. Nonetheless, we emphasize the significant uncertainties in these trends due to limited data coverage, irregular sampling intervals as well as the definition of the endmembers themselves within the mixing model.

4. Discussion

4.1. Interhemispheric Asymmetry in Dense Water Formation

The present analysis, being globally consistent, highlights the different roles of MW and SIM are in the formation of deep waters filling the northern and southern hemisphere ocean basins. The North Atlantic deep basin is filled by waters that carry an evaporative signal (negative MW) partially compensated by sea ice meltwater (positive SIM), whereas the Southern Ocean abyssal basin is filled by waters freshened due to precipitation (positive MW) and partially compensated by brine (negative SIM; Figure 6). These distinct signatures are carried and exported into the ocean interior.

We see that the freshwater loss (or salinity increase) required for high latitude dense water formation is provided by evaporation (preconditioning the surface waters through the length of the Atlantic) in the Subpolar North Atlantic and brine rejection through sea ice formation in the Southern Hemisphere. Although sea ice processes might bias our definition of the meteoric endmember and be propagated to the MW and SIM estimates, especially in the Subpolar North Atlantic, the combination of $\delta^{18}O$ with $\delta^{2}H$ also indicates an evaporative signal in the waters formed here (Sodemann et al., 2024). We further expect that the preconditioning of the relatively high salinity surface AW entering the Subpolar North Atlantic itself inhibits sea ice formation (See α oceans in Carmack, 2007; Stewart & Haine, 2016). When these high-salinity waters cool down they tend to overturn and mix, ventilating the deep ocean and eroding the near-surface cooling that would be required for sea ice to form (See β oceans in Carmack, 2007; Stewart & Haine, 2016). In the northern hemisphere, sea ice is mostly formed in few regions in the Arctic associated with the Arctic river run-off where density stratification is dominated by salinity, that is, PSW in the Arctic halocline (Negative SIM; Figure 8c). These waters are too fresh for any gain in salinity (density) to result in DW. Only the densest part of DW contains traces of sea ice formation (Figure 8c). On the contrary, in the Southern Ocean, LCDW (fresher than the north Atlantic AW) upwells in the Southern Hemisphere, around Antarctica. The salinity in LCDW is low enough for sea ice formation (negative SIM) to significantly increase the density of surface waters, enabling the formation of dense water masses such as ISW, the precursor of AABW (Figure 7c). Thus, low salinity LCDW preconditions sea ice formation in the Southern Ocean, which in turns affects the formation and export of AABW (Haumann et al., 2016; Zhou et al., 2023).

4.2. Sensitivity and Uncertainty

Endmember properties are assumed to be both known and time-invariant. To quantify the uncertainty regarding these assumptions we first quantify the sensitivity of the estimated relative contributions (for OC, MW, and SIM) with respect to the endmember properties. Then, we scale these sensitivities by the uncertainty in the endmember properties.

Each of the estimated endmember fractions (x in Equation 4) has a unique sensitivity with respect to the chosen combination of endmember properties ($\mathbf{A}$). An efficient way of calculating this is through the adjoint of $\mathbf{A}$, which is equal to the partial derivative of $\mathbf{A}$ with respect to x, and is calculated with the Kronecker product of x and $\mathbf{A}$

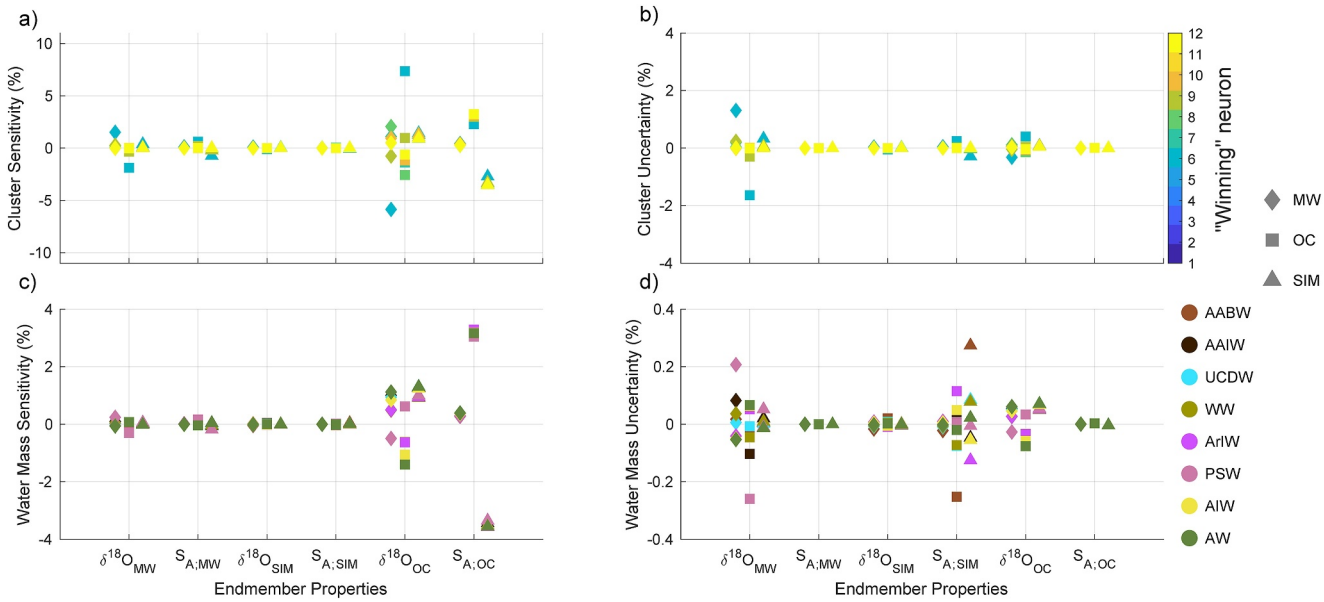

Figure 9. Sensitivity of water masses to changes in the endmember properties in A (Equation 4) (a–b). Uncertainty in the endmember mass fractions obtained by scaling the sensitivity according to the uncertainty in the endmember properties (c–d). Symbols indicate the change in each endmember with respect to a change in the defined properties in the *x*-axis. Colors in indicate the different water masses (c–d).

(Equation 5 and Appendix A). The resulting sensitivity matrix, **S**, in combination with the bootstrapping and the range in values in literature, provides a range of uncertainty for our estimates. The sensitivity matrix reflects the additions to the endmember fractions with respect to a one-unit increment in the endmember properties, which on itself provides insights about the mixing model and the importance of each property (Figures 9a and 9c). The uncertainty is calculated by scaling the sensitivity according to the uncertainty in the endmember properties (Figures 9b and 9d).

Overall, polar clusters are the least sensitive to the endmember properties (Figure 9a). This is because of the geometry of the mixing model for these clusters, as the MW endmember is further to the SIM endmember and showcases the use of $\delta^{18}O$ as a freshwater tracer at these latitudes. All clusters are most sensitive to the OC endmembers properties, as they sit close to that endmember (see high contribution of OC in Figures 7a and 8a). Because all data-points have their unique sensitivity, the selection of endmember properties is determinant not only for the quantification but also the pattern. The strong sensitivity to the OC endmember also highlights the relative nature of this approach, for example, referencing OC salinity to 34.8 (instead of 34.7) would remove about 0.4% of SIM to most of the clusters. Referencing the OC endmember to the mean interior ocean, $S_A = 34.7$, and the corresponding $\delta^{18}O$ intercept for that salinity, our approach estimates changes in the freshwater budget through the entire pathway of those waters. This steady-state global perspective is a compromise that might differ from local freshwater budgets that are referenced to specific water masses. These sensitivities are smaller for the endmember fractions in the water masses (Figure 9c). Here as well, fractional estimates are most sensitive to the OC endmember properties.

Table 3
Uncertainty Related to the Definition of the Endmember Properties

	$\delta^{18}O$ (‰)	S_A (g kg^{-1})
Meteoric water (MW)	±0.78[a]	-
Sea ice meltwater (SIM)	±0.6[b]	±7[c]
Ocean water (OC)	$\pm\delta^{18}O_{S=43.701}$[a]	±0.001[d]

Note. Meteoric water $\delta^{18}O$ uncertainty is obtained from the bootstrapping of the self-organizing map as the averaged of all clusters, $\delta^{18}O_S = 43.701$ refers to the $\delta^{18}O$ intercept at salinity = 43.701 from the S-$\delta^{18}O$ regressions in each of the clusters. [a]This study. [b]Ekwurzel et al. (2001), Eicken (1998). [c]Eicken (1992), Cox and Weeks (1974). [d]Skliris et al. (2014).

However, this sensitivity is not directly translated into uncertainty in our estimates, as it has to be scale by the uncertainty in the endmember properties in **A** (Table 3). The ocean interior salinity remains nearly constant at climatic relevant scales (e.g., Holland, 1972). Only the recently ventilated regions (with imprints of Chlorofluorocarbon-11, an anthropogenic tracer) have been subjected to significant changes in salinity over time (Durack & Wijffels, 2010), and have already been subjected to the hydrological cycle. Below 1,500 m, only in the Atlantic a small change has been observed in the last 60 year of the order of 0.001 (Skliris et al., 2014). Using this value to scale the sensitivity, the resulting uncertainty related to variation on S_{OC} for both clusters and water masses is negligible (Figures 9b and 9d). There are far less

observations of $\delta^{18}O$ in the interior ocean than for salinity, with very limited knowledge regarding its variability (Meredith et al., 1999), and even the state (Gebbie & Huybers, 2010; LeGrande & Schmidt, 2006). For the 0.001 change in the S_{OC} endmember, the corresponding change in $\delta^{18}O$ intercept is calculated, and is used as the uncertainty in ($\delta^{18}O_{OC}$). After scaling the sensitivity, the uncertainty in our estimates regarding this property results to be small.

The largest uncertainty in the clusters is the uncertainty in the isotopic signature of MW, $\delta^{18}O_{MW}$, which we calculate the uncertainty by bootstrapping the SOM (Figure 4). After scaling the sensitivity, this is still smallest at polar clusters. Regarding the uncertainty in the water masses, the largest uncertainty is related to the salinity of the sea ice. Although the sensitivity to this endmember property is small, its uncertainty is large. Literature values range between above 14 to below 4 g kg^{-1} in the Weddell Sea first-year ice (Eicken, 1992), and 2–3 g kg^{-1} in different types of Arctic multiyear ice (Cox & Weeks, 1974). We therefore upscale the sensitivity by a factor of $\pm$7 g kg^{-1} to cover the this entire salinity range (as S_{SIM} was set at 7). The second largest uncertainty is given by $\delta^{18}O_{MW}$. Nevertheless, these uncertainties are an order of magnitude smaller than the estimates of endmember contributions (Figures 7 and 8 and Figure S3 and S4 in Supporting Information S1).

Regarding the isotopic signature of sea ice, fractionation varies with the ice growth rate, with theoretical estimates range from 1.5‰ to 2.7‰ in the Arctic (Ekwurzel et al., 2001), and up to 2.7‰ observed in the Weddell Sea (Eicken, 1998). Based on these values, we set the uncertainty in $\delta^{18}O_{SIM}$ to be $\pm$0.6‰, which results in a negligible uncertainty in our endmember mass fractions.

Although the estimated uncertainties are an order of magnitude lower than the endmember contributions, these sensitivity highlight the importance of $\delta^{18}O$ measurements. First, the estimates of SIM and OC contributions are highly sensitive to the ocean endmember $\delta^{18}O$. Although here we assume that co-evolves with salinity, there is not enough interior ocean observations to verify this. The uncertainty in the MW endmember $\delta^{18}O$ translates directly into the uncertainty in the endmember contributions. Part of this uncertainty can be related to the seasonal cycle or transient changes in the hydrological cycle (Breitkreuz et al., 2018) but also to the fact that sea ice processes may bias the estimate of $\delta^{18}O_{MW}$ based on salinity-$\delta^{18}O$ relationships.

5. Conclusions

This study showcases the utility of $\delta^{18}O$, not only for constraining regional freshwater budgets, but also at global scales. We disentangle the ocean freshwater sources based on salinity-$\delta^{18}O$ relationships by removing at each time the leading mode of variability: first the MW isotopic signature by identifying the OC-MW mixing line, and then the effect of sea ice as its residuals. We circumvent the difficulties regarding the identification of the MW isotopic signature by utilizing an unsupervised machine learning technique, the SOM that clusters and extracts spatial and temporal patterns in the data. Co-located measurements of conservative temperature (θ), absolute salinity (S_A) and $\delta^{18}O$ are used as input for the SOM. The resulting clusters are classified according to these co-variability of these properties in close agreement with the current knowledge of water masses. The $\delta^{18}O_{MW}$ concentration is then estimated by regressing $\delta^{18}O$ and S for each of the clusters. Overall, the resulting $\delta^{18}O_{MW}$ is in good agreement with the concentrations measured directly in precipitation from the GNIP, but differs in those places where advection dominates the freshwater budget over local precipitation.

By identifying the regionally variant $\delta^{18}O_{MW}$, we complete the three endmember mixing model to quantify the contribution of MW (precipitation/evaporation) and SIM (sea ice melt/brine rejection). Our estimates represent the freshwater budget through the entire pathway of those waters, with the interior ocean as a reference and therefore may not align with local freshwater budgets that are referenced to specific water masses. In the Arctic, the surface (<200 m) freshwater budget is dominated by MW resulting from the runoff from Arctic river, whereas the SIM follows the sea ice edge, and brine reflect the sea ice formation in the Arctic polynyas. Waters at greater depths (>200 m) carry evaporative signal related to inflowing AW as well as sea ice melting. The surface in the Southern Ocean is also dominated by MW, but to a lesser extent, whereas SIM distribution is more patchy. In contrast to the northern hemisphere, greater depths (>200 m) in the Southern Ocean feature precipitation (and possibly glacier melt at >1,500 m), as well as brine related to the role of sea ice in the formation of dense waters here such as ISW and AABW.

Collapsing MW and SIM estimates in θ-S space provides insight on the role of MW and SIM in the formation and transformation of water masses and their changes over time. Significant trends estimated in θ-S space show that AABW has freshened during 1980–2023 due to less sea ice being formed rather than more MW (glacier melt) being injected. In the Arctic and Subpolar North Atlantic, trends show a significant increase in sea ice melt in most of the spectrum of PSW. These changes are in agreement with previous studies, but such changes are for the first time been reported based on δ^{18}O. These changes are more coherent in δ^{18}O than salinity, which might be related to the earlier emergence of anthropogenic-forced signals in δ^{18}O and depicts the usefulness of δ^{18}O to understand the ongoing changes in the ocean freshwater budget.

One of the main limitations of this study is the data sparsity of δ^{18}O which hinders the interpretation of the observed SIM and MW changes in water masses. The distinct isotopic fingerprints of MW and SIM that are transported across the interior can, however, be used for reconstructing past freshwater fluxes and their role in shaping dense water formation. Building on the framework proposed by Gebbie and Huybers (2019), who used water mass transit times from an inverse circulation model to reconstruct the surface temperature the Little Ice Age, a similar approach could be applied to the MW and SIM contributions estimated here. By combining modern observations with inverse modeling techniques that account for the advection and mixing of water masses, it may be possible to project backwards the isotopic composition of deep waters to their surface origins. This would allow for the reconstruction of past MW and SIM distributions, offering insights into how freshwater forcing and dense water formation have co-evolved over centennial timescales. Such reconstructions could provide critical context for assessing the sensitivity of the overturning circulation to past and future climate variability.

Appendix A: Sensitivity Estimation via the Kronecker Product

The solution for x in Equation 4 is found by inverting $\mathbf{A}$ and multiplying by a vector b containing the observations:

$$x = \mathbf{A}^{-1}b \tag{A1}$$

where the sensitivity of the mixing model is obtained by differentiating x with respect to $\mathbf{A}$ through the Kronecker product (Neudecker, 1969), where b is constant, so that

$$dx = d\left(\mathbf{A}^{-1}b\right) = d\left(\mathbf{A}^{-1}\right)b \tag{A2}$$

and we know from general rules of matrix differentiation that

$$d\left(\mathbf{A}^{-1}\right) = -\mathbf{A}^{-1}(d\mathbf{A})\mathbf{A}^{-1} \tag{A3}$$

Substituting Equation A3 into Equation A2 and vectorizing both sides we obtain the expression

$$\mathrm{vec}\,(dx) = \mathrm{vec}\left(-\mathbf{A}^{-1}(d\mathbf{A})\mathbf{A}^{-1}b\right) \tag{A4}$$

where RHS of Equation A4 now follows the properties of the Kronecker product (Neudecker, 1969):

$$\mathrm{vec}\,(\mathbf{ABC}) = \left(\mathbf{C}^T \otimes \mathbf{A}\right)\mathrm{vec}\,(\mathbf{B}) \tag{A5}$$

Applying this rule to Equation A3 and substituting $\mathbf{A}^{-1}b$ by x we obtain:

$$\mathrm{vec}\,(dx) = \mathrm{vec}\left(-\mathbf{A}^{-1}(d\mathbf{A})x\right) = \left(-x^T \otimes \mathbf{A}^{-1}\right)\mathrm{vec}\,(d\mathbf{A}) \tag{A6}$$

which can be rearranged to the expression in Equation 5 in the main text,

$$S = \frac{dx}{d\mathbf{A}} = -x^T \otimes \mathbf{A}^{-1} \tag{A7}$$

where $\otimes$ denotes the Kronecker product between $\mathbf{A}$ and x^T and results in a 3×9 matrix for each element in x with the sensitivity of such element with respect to all the properties in $\mathbf{A}$.

Data Availability Statement

The meteoric water and sea ice meltwater fractions estimated in this study, as well as the MW $\delta^{18}O$ are available in Zenodo (https://zenodo.org/records/16992714) and the $\delta^{18}O$ data set used in this study are already available online: NASA GISS (https://data.giss.nasa.gov/o18data/), CISE-LOCEAN (https://doi.org/10.17882/71186) and individual cruise data available at the British Oceanographic Data Centre (https://www.bodc.ac.uk/). The $\delta^{18}O$ concentration in precipitation is available at the International Atomic Energy Agency (https://www.iaea.org/services/networks/gnip).

Acknowledgments

We first would like to thank everybody involved in the collection, analysis, and publication of $\delta^{18}O$ measurements that made this study possible. We also thank three anonymous reviewers for their insightful feedback that helped improve this manuscript. We would also like to thank Laura J. Dietrich for stimulating discussions regarding $\delta^{18}O$ in precipitation and Rachael Sanders for pointing us towards additional $\delta^{18}O$ data in seawater. This research was supported by OCEAN: ICE, which is co-funded by the European Union, Horizon Europe Funding Program for research and innovation under grant agreement Nr. 101060452 and by UK Research and Innovation. O:I Contribution number 13. FJ was funded by the UK National Capability project Atlantis under NERC grant NE/Y005589/1. GG was supported by U.S. National Science Foundation grant OCE-2122805. The participation of MM was part-funded by the Natural Environment Research Council via the BIOPOLE project.

References

Allan, D., & Allan, R. P. (2024). Odden ice melt linked to Labrador Sea ice expansions and the Great Salinity Anomalies of 1970–1995. *Journal of Geophysical Research: Oceans*, *129*(4), e2023JC019988. https://doi.org/10.1029/2023JC019988

Bauch, D., Erlenkeuser, H., & Andersen, N. (2005). Water mass processes on Arctic shelves as revealed from $\delta^{18}O$ of H_2O. *Global and Planetary Change*, *48*(1), 165–174. https://doi.org/10.1016/j.gloplacha.2004.12.011

Bauch, D., Schlosser, P., & Fairbanksl, R. (1995). Freshwater balance and the sources of deep and bottom waters in the Arctic Ocean inferred from the distribution of H2180. *Progress in Oceanography*, *35*(1), 53–80. https://doi.org/10.1016/0079-6611(95)00005-2

Belkin, I. M. (2004). Propagation of the "Great Salinity Anomaly" of the 1990s around the northern North Atlantic. *Geophysical Research Letters*, *31*(8), L08306. https://doi.org/10.1029/2003GL019334

Benway, H. M., & Mix, A. C. (2004). Oxygen isotopes, upper-ocean salinity, and precipitation sources in the eastern tropical Pacific. *Earth and Planetary Science Letters*, *224*(3), 493–507. https://doi.org/10.1016/j.epsl.2004.05.014

Biló, T. C., Straneo, F., Holte, J., & Le Bras, I. a.-A. (2022). Arrival of new great salinity Anomaly weakens convection in the Irminger Sea. *Geophysical Research Letters*, *49*(11), e2022GL098857. https://doi.org/10.1029/2022GL098857

Boisvert, L. N., Webster, M. A., Petty, A. A., Markus, T., Cullather, R. I., & Bromwich, D. H. (2020). Intercomparison of precipitation estimates over the Southern Ocean from atmospheric reanalyses. *Journal of Climate*, *33*(24), 10627–10651. https://doi.org/10.1175/JCLI-D-20-0044.1

Bosse, A., Fer, I., Søiland, H., & Rossby, T. (2018). Atlantic water transformation along its poleward pathway across the Nordic Seas. *Journal of Geophysical Research: Oceans*, *123*(9), 6428–6448. https://doi.org/10.1029/2018JC014147

Bowen, G. J., & Revenaugh, J. (2003). Interpolating the isotopic composition of modern meteoric precipitation. *Water Resources Research*, *39*(10). https://doi.org/10.1029/2003WR002086

Boyer, T., Levitus, S., Antonov, J., Locarnini, R., Mishonov, A., Garcia, H., & Josey, S. A. (2007). Changes in freshwater content in the North Atlantic Ocean 1955–2006. *Geophysical Research Letters*, *34*(16), L16603. https://doi.org/10.1029/2007GL030126

Breitkreuz, C., Paul, A., Kurahashi-Nakamura, T., Losch, M., & Schulz, M. (2018). A dynamical reconstruction of the global monthly mean oxygen isotopic composition of seawater. *Journal of Geophysical Research: Oceans*, *123*(10), 7206–7219. https://doi.org/10.1029/2018JC014300

Brown, P. J., Meredith, M. P., Jullion, L., Garabato, A. N., Torres-Valdés, S., Holland, P., et al. (2014). Freshwater fluxes in the Weddell Gyre: Results from $\delta^{18}O$. *Philosophical Transactions of the Royal Society A: Mathematical, Physical and Engineering Sciences*, *372*(2019), 20130298. https://doi.org/10.1098/rsta.2013.0298

Carmack, E. C. (2007). The alpha/beta ocean distinction: A perspective on freshwater fluxes, convection, nutrients and productivity in high-latitude seas. *Deep Sea Research Part II: Topical Studies in Oceanography*, *54*(23), 2578–2598. https://doi.org/10.1016/j.dsr2.2007.08.018

Carmack, E. C., & Foster, T. (1977). Water masses and circulation in the Weddell Sea. In *Proceedings of the Polar Ocean Conference* (Vol. 1974, pp. 151–165).

Conroy, J. L., Thompson, D. M., Cobb, K. M., Noone, D., Rea, S., & Legrande, A. N. (2017). Spatiotemporal variability in the $\delta^{18}O$-salinity relationship of seawater across the tropical Pacific Ocean. *Paleoceanography*, *32*(5), 484–497. https://doi.org/10.1002/2016PA003073

Cornish, S. B., Johnson, H. L., Mallett, R. D. C., Dörr, J., Kostov, Y., & Richards, A. E. (2022). Rise and fall of sea ice production in the Arctic Ocean's ice factories. *Nature Communications*, *13*(1), 7800. https://doi.org/10.1038/s41467-022-34785-6

Cox, G. F. N., & Weeks, W. F. (1974). Salinity variations in sea ice. *Journal of Glaciology*, *13*(67), 109–120. https://doi.org/10.3189/S0022143000023418

Craig, H., & Gordon, L. (1965). Deuterium and oxygen 18 variations in the ocean and the marine atmosphere, stable isotopes in oceanographic studies and paleotemperatures. In E. Tongiori (Ed.), *Proceedings of the third Spoleto conference, Spoleto, Italy* (pp. 9–130).

Davila, X., Gebbie, G., Brakstad, A., Lauvset, S. K., McDonagh, E. L., Schwinger, J., & Olsen, A. (2022). How is the ocean anthropogenic carbon reservoir filled? *Global Biogeochemical Cycles*, *36*(5), e2021GB007055. https://doi.org/10.1029/2021GB007055

De Lavergne, C., Palter, J. B., Galbraith, E. D., Bernardello, R., & Marinov, I. (2014). Cessation of deep convection in the open Southern Ocean under anthropogenic climate change. *Nature Climate Change*, *4*(4), 278–282. https://doi.org/10.1038/nclimate2132

Dickson, R. R., Meincke, J., Malmberg, S.-A., & Lee, A. J. (1988). The "great salinity anomaly" in the Northern North Atlantic 1968–1982. *Progress in Oceanography*, *20*(2), 103–151. https://doi.org/10.1016/0079-6611(88)90049-3

Durack, P. J., & Wijffels, S. E. (2010). Fifty-Year trends in Global Ocean salinities and their relationship to broad-scale warming. *Journal of Climate*, *23*(16), 4342–4362. https://doi.org/10.1175/2010JCLI3377.1

Eicken, H. (1992). Salinity profiles of Antarctic sea ice: Field data and model results. *Journal of Geophysical Research*, *97*(C10), 15545–15557. https://doi.org/10.1029/92JC01588

Eicken, H. (1998). Deriving modes and rates of ice growth in the Weddell Sea from microstructural, salinity and stable-isotope data. In M. O. Jeffries (Ed.), *Antarctic research series* (pp. 89–122). American Geophysical Union. https://doi.org/10.1029/AR074p0089

Ekwurzel, B., Schlosser, P., Mortlock, R. A., Fairbanks, R. G., & Swift, J. H. (2001). River runoff, sea ice meltwater, and Pacific water distribution and mean residence times in the Arctic Ocean. *Journal of Geophysical Research*, *106*(C5), 9075–9092. https://doi.org/10.1029/1999JC000024

Fairbanks, R. G. (1982). The origin of continental shelf and slope water in the New York Bight and Gulf of Maine: Evidence from $H_2{}^{18}O/H_2{}^{16}O$ ratio measurements. *Journal of Geophysical Research*, *87*(C8), 5796–5808. https://doi.org/10.1029/JC087iC08p05796

Frew, R. D., Dennis, P. F., Heywood, K. J., Meredith, M. P., & Boswell, S. M. (2000). The oxygen isotope composition of water masses in the northern North Atlantic. *Deep Sea Research Part I: Oceanographic Research Papers*, *47*(12), 2265–2286. https://doi.org/10.1016/S0967-0637(00)00023-6

Galewsky, J., Steen-Larsen, H. C., Field, R. D., Worden, J., Risi, C., & Schneider, M. (2016). Stable isotopes in atmospheric water vapor and applications to the hydrologic cycle. *Reviews of Geophysics*, *54*(4), 809–865. https://doi.org/10.1002/2015RG000512

Gebbie, G., & Huybers, P. (2010). Total Matrix intercomparison: A method for determining the geometry of water-mass pathways. *Journal of Physical Oceanography*, *40*(8), 1710–1728. https://doi.org/10.1175/2010jpo4272.1

Gebbie, G., & Huybers, P. (2019). The little Ice Age and 20th-century deep Pacific cooling. *Science*, *74*(January), 70–74. https://doi.org/10.1126/science.aar8413

Glessmer, M. S., Eldevik, T., Våge, K., Øie Nilsen, J. E., & Behrens, E. (2014). Atlantic origin of observed and modelled freshwater anomalies in the Nordic Seas. *Nature Geoscience*, *7*(11), 801–805. https://doi.org/10.1038/ngeo2259

Granskog, M. A., Stedmon, C. A., Dodd, P. A., Amon, R. M. W., Pavlov, A. K., De Steur, L., & Hansen, E. (2012). Characteristics of colored dissolved organic matter (CDOM) in the Arctic outflow in the Fram Strait: Assessing the changes and fate of terrigenous CDOM in the Arctic Ocean. *Journal of Geophysical Research*, *117*(C12), 2012JC008075. https://doi.org/10.1029/2012JC008075

Haumann, F. A., Gruber, N., Münnich, M., Frenger, I., & Kern, S. (2016). Sea-ice transport driving Southern Ocean salinity and its recent trends. *Nature*, *537*(7618), 89–92. https://doi.org/10.1038/nature19101

Hennig, A. N., Mucciarone, D. A., Jacobs, S. S., Mortlock, R. A., & Dunbar, R. B. (2024). Meteoric water and glacial melt in the southeastern Amundsen Sea: A time series from 1994 to 2020. *The Cryosphere*, *18*(2), 791–818. https://doi.org/10.5194/tc-18-791-2024

Holland, H. D. (1972). The geologic history of sea water—An attempt to solve the problem. *Geochimica et Cosmochimica Acta*, *36*(6), 637–651. https://doi.org/10.1016/0016-7037(72)90108-1

Holliday, N. P., Hughes, S. L., Bacon, S., Beszczynska-Möller, A., Hansen, B., Lavín, A., et al. (2008). Reversal of the 1960s to 1990s freshening trend in the northeast North Atlantic and Nordic Seas. *Geophysical Research Letters*, *35*(3), L21S02. https://doi.org/10.1029/2007GL032675

Jebri, F., Srokosz, M., Jacobs, Z. L., Nencioli, F., & Popova, E. (2022). Earth observation and machine learning reveal the dynamics of productive upwelling regimes on the Agulhas Bank. *Frontiers in Marine Science*, *9*, 872515. https://doi.org/10.3389/fmars.2022.872515

Jenkins, A. (1999). The impact of melting ice on ocean waters. *Journal of Physical Oceanography*, *29*(9), 2370–2381. https://doi.org/10.1175/1520-0485(1999)029<2370:tiomio>2.0.co;2

Jouini, M., Béranger, K., Arsouze, T., Beuvier, J., Thiria, S., Crépon, M., & Taupier-Letage, I. (2016). The Sicily channel surface circulation revisited using a neural clustering analysis of a high-resolution simulation. *Journal of Geophysical Research: Oceans*, *121*(7), 4545–4567. https://doi.org/10.1002/2015JC011472

Khan, S. A., Kjær, K. H., Bevis, M., Bamber, J. L., Wahr, J., Kjeldsen, K. K., et al. (2014). Sustained mass loss of the northeast Greenland ice sheet triggered by regional warming. *Nature Climate Change*, *4*(4), 292–299. https://doi.org/10.1038/nclimate2161

Kim, H., & Timmermann, A. (2024). Seawater oxygen isotopes as a tool for monitoring future meltwater from the Antarctic ice-sheet. *Communications Earth & Environment*, *5*(1), 1–11. https://doi.org/10.1038/s43247-024-01514-4

Kohonen, T. (1982). Self-organized formation of topologically correct feature maps. *Biological Cybernetics*, *43*(1), 59–69. https://doi.org/10.1007/BF00337288

Kohonen, T. (2014). *MATLAB implementations and applications of the self-organizing map*. Unigrafia Oy.

Konecky, B. L., Noone, D. C., & Cobb, K. M. (2019). The influence of competing hydroclimate processes on stable isotope ratios in tropical rainfall. *Geophysical Research Letters*, *46*(3), 1622–1633. https://doi.org/10.1029/2018GL080188

Kopec, B. G., Klein, E. S., Feldman, G. C., Pedron, S. A., Bailey, H., Causey, D., et al. (2024). Arctic freshwater sources and ocean mixing relationships revealed with seawater isotopic tracing. *Journal of Geophysical Research: Oceans*, *129*(7), e2023JC020583. https://doi.org/10.1029/2023JC020583

LeGrande, A. N., & Schmidt, G. A. (2006). Global gridded data set of the oxygen isotopic composition in seawater. *Geophysical Research Letters*, *33*(12), L12604. https://doi.org/10.1029/2006GL026011

Li, Q., England, M. H., Hogg, A. M., Rintoul, S. R., & Morrison, A. K. (2023). Abyssal ocean overturning slowdown and warming driven by Antarctic meltwater. *Nature*, *615*(7954), 841–847. https://doi.org/10.1038/s41586-023-05762-w

Liu, J., Chen, S., Zhou, Z., & Wu, T. (2016). An anomaly detection algorithm of cloud platform based on self-organizing maps. *Mathematical Problems in Engineering*, *2016*, 1–9. https://doi.org/10.1155/2016/3570305

Liu, Y., & Weisberg, R. H. (2005). Patterns of ocean current variability on the West Florida Shelf using the self-organizing map. *Journal of Geophysical Research*, *110*(C6), 12. https://doi.org/10.1029/2004JC002786

Liu, Y., Weisberg, R. H., & Mooers, C. N. K. (2006). Performance evaluation of the self-organizing map for feature extraction. *Journal of Geophysical Research*, *111*(C5), C05018. https://doi.org/10.1029/2005JC003117

López-Rubio, E., & Díaz Ramos, A. (2014). Grid topologies for the self-organizing map. *Neural Networks*, *56*, 35–48. https://doi.org/10.1016/j.neunet.2014.05.001

Marsland, S. J., & Wolff, J.-O. (2001). On the sensitivity of Southern Ocean sea ice to the surface freshwater flux: A model study. *Journal of Geophysical Research*, *106*(C2), 2723–2741. https://doi.org/10.1029/2000JC900086

McConnaughey, T. (1989). ^{13}C and ^{18}O isotopic disequilibrium in biological carbonates: I. Patterns. *Geochimica et Cosmochimica Acta*, *53*(1), 151–162. https://doi.org/10.1016/0016-7037(89)90282-2

McDougall, T. J., & Barker, P. M. (2011). *Getting started with TEOS-10 and the Gibbs seawater (GSW) oceanographic toolbox*. SCOR/IAPSO WG127.

Melling, H., & Moore, R. M. (1995). Modification of halocline source waters during freezing on the Beaufort Sea Shelf: Evidence from oxygen isotopes and dissolved nutrients. *Continental Shelf Research*, *15*(1), 89–113. https://doi.org/10.1016/0278-4343(94)p1814-r

Meredith, M. P., Brandon, M. A., Wallace, M. I., Clarke, A., Leng, M. J., Renfrew, I. A., et al. (2008). Variability in the freshwater balance of northern Marguerite Bay, Antarctic Peninsula: Results from $\delta^{18}O$. *Deep Sea Research Part II: Topical Studies in Oceanography*, *55*(3–4), 309–322. https://doi.org/10.1016/j.dsr2.2007.11.005

Meredith, M. P., Falk, U., Bers, A. V., Mackensen, A., Schloss, I. R., Ruiz Barlett, E., et al. (2018). Anatomy of a glacial meltwater discharge event in an Antarctic cove. *Philosophical transactions. Series A, Mathematical, physical, and engineering sciences*, *376*(2122), 20170163. https://doi.org/10.1098/rsta.2017.0163

Meredith, M. P., Grose, K. E., McDonagh, E. L., Heywood, K. J., Frew, R. D., & Dennis, P. F. (1999). Distribution of oxygen isotopes in the water masses of Drake Passage and the South Atlantic. *Journal of Geophysical Research*, *104*(C9), 20949–20962. https://doi.org/10.1029/98JC02544

Meredith, M. P., Wallace, M. I., Stammerjohn, S. E., Renfrew, I. A., Clarke, A., Venables, H. J., et al. (2010). Changes in the freshwater composition of the upper ocean west of the Antarctic Peninsula during the first decade of the 21st century. *Progress in Oceanography*, *87*(1–4), 127–143. https://doi.org/10.1016/j.pocean.2010.09.019

Merino, N., Jourdain, N. C., Le Sommer, J., Goosse, H., Mathiot, P., & Durand, G. (2018). Impact of increasing Antarctic glacial freshwater release on regional sea-ice cover in the Southern Ocean. *Ocean Modelling*, *121*, 76–89. https://doi.org/10.1016/j.ocemod.2017.11.009

Merino, N., Le Sommer, J., Durand, G., Jourdain, N. C., Madec, G., Mathiot, P., & Tournadre, J. (2016). Antarctic icebergs melt over the Southern Ocean: Climatology and impact on sea ice. *Ocean Modelling*, *104*, 99–110. https://doi.org/10.1016/j.ocemod.2016.05.001

Millet, B., Gray, W. R., de Lavergne, C., & Roche, D. M. (2024). Oxygen isotope constraints on the ventilation of the modern and glacial Pacific. *Climate Dynamics*, *62*(1), 649–664. https://doi.org/10.1007/s00382-023-06910-8

Murray, N. K., Muñoz, A. R., & Conroy, J. L. (2023). Machine learning solutions to regional surface Ocean δ^{18}O-Salinity relationships for paleoclimatic reconstruction. *Paleoceanography and Paleoclimatology*, *38*(9), e2023PA004612. https://doi.org/10.1029/2023PA004612

Mysak, L. A., Manak, D. K., & Marsden, R. F. (1990). Sea-ice anomalies observed in the Greenland and Labrador seas during 1901–1984 and their relation to an interdecadal Arctic climate cycle. *Climate Dynamics*, *5*(2), 111–133. https://doi.org/10.1007/BF00207426

Nelson, M., Straneo, F., Purkey, S. G., & de Jong, M. F. (2024). Delayed recovery of the Irminger Interior from cooling in 2015 due to widespread buoyancy loss and suppressed restratification. *Geophysical Research Letters*, *51*(2), e2023GL106501. https://doi.org/10.1029/2023GL106501

Neudecker, H. (1969). Some theorems on matrix differentiation with special reference to kronecker matrix products. *Journal of the American Statistical Association*, *64*(327), 953–963. https://doi.org/10.1080/01621459.1969.10501027

Newsom, E., Zanna, L., Khatiwala, S., & Gregory, J. M. (2020). The influence of warming patterns on passive ocean heat uptake. *Geophysical Research Letters*, *47*(18), e2020GL088429. https://doi.org/10.1029/2020GL088429

Nicholls, K. W., Østerhus, S., Makinson, K., Gammelsrød, T., & Fahrbach, E. (2009). Ice-ocean processes over the continental shelf of the southern Weddell Sea, Antarctica: A review. *Reviews of Geophysics*, *47*(3), RG3003. https://doi.org/10.1029/2007RG000250

Orsi, A. H., Whitworth, T., & Nowlin, W. D. (1995). On the meridional extent and fronts of the Antarctic Circumpolar Current. *Deep Sea Research Part I: Oceanographic Research Papers*, *42*(5), 641–673. https://doi.org/10.1016/0967-0637(95)00021-W

Östlund, H. G., & Hut, G. (1984). Arctic Ocean water mass balance from isotope data. *Journal of Geophysical Research*, *89*(C4), 6373–6381. https://doi.org/10.1029/JC089iC04p06373

Reusch, D. B., Alley, R. B., & Hewitson, B. C. (2005). Relative performance of self-organizing maps and principal component analysis in pattern extraction from synthetic climatological data. *Polar Geography*, *29*(3), 188–212. https://doi.org/10.1080/789610199

Reverdin, G., Waelbroeck, C., Pierre, C., Akhoudas, C., Aloisi, G., Benetti, M., et al. (2022). The CISE-LOCEAN seawater isotopic database (1998–2021). *Earth System Science Data*, *14*(6), 2721–2735. https://doi.org/10.5194/essd-14-2721-2022

Rignot, E., Velicogna, I., Van Den Broeke, M. R., Monaghan, A., & Lenaerts, J. T. M. (2011). Acceleration of the contribution of the Greenland and Antarctic ice sheets to sea level rise: Acceleration of ice sheet loss. *Geophysical Research Letters*, *38*(5), L05503. https://doi.org/10.1029/2011GL046583

Risebrobakken, B., Jansen, E., Andersson, C., Mjelde, E., & Hevrøy, K. (2003). A high-resolution study of Holocene paleoclimatic and paleoceanographic changes in the Nordic Seas. *Paleoceanography*, *18*(1), 1017. https://doi.org/10.1029/2002PA000764

Rohling, E. J. (2013). Oxygen isotope composition of seawater. In S. A. Elias & C. J. Mock (Eds.), *Encyclopedia of Quaternary science* (2nd ed., pp. 915–922). Elsevier. Retrieved from https://www.sciencedirect.com/science/article/pii/B9780444536433002934

Rohling, E. J., & Bigg, G. R. (1998). Paleosalinity and δ18O: A critical assessment. *Journal of Geophysical Research*, *103*(C1), 1307–1318. https://doi.org/10.1029/97JC01047

Rudels, B., Björk, G., Nilsson, J., Winsor, P., Lake, I., & Nohr, C. (2005). The interaction between waters from the Arctic Ocean and the Nordic Seas north of Fram Strait and along the East Greenland Current: Results from the Arctic Ocean-02 Oden expedition. *Journal of Marine Systems*, *55*(1), 1–30. https://doi.org/10.1016/j.jmarsys.2004.06.008

Schmidt, G. A., Bigg, G. R., & Rohling, E. J. (1999). Global seawater oxygen-18 database—V1.22. Retrieved from https://data.giss.nasa.gov/o18data/

Schumann, E. H. (1999). Wind-driven mixed layer and coastal upwelling processes off the south coast of South Africa. *Journal of Marine Research*, *57*(4), 671–691. https://doi.org/10.1357/002224099321549639

Silvano, A., Purkey, S., Gordon, A. L., Castagno, P., Stewart, A. L., Rintoul, S. R., et al. (2023). Observing Antarctic bottom water in the Southern Ocean. *Frontiers in Marine Science*, *10*, 1221701. https://doi.org/10.3389/fmars.2023.1221701

Simon, M. H., Muschitiello, F., Tisserand, A. A., Olsen, A., Moros, M., Perner, K., et al. (2020). A multi-decadal record of oceanographic changes of the past ~165 years (1850–2015 AD) from Northwest of Iceland. *PLoS One*, *15*(9), e0239373. https://doi.org/10.1371/journal.pone.0239373

Skliris, N., Marsh, R., Josey, S. A., Good, S. A., Liu, C., & Allan, R. P. (2014). Salinity changes in the World Ocean since 1950 in relation to changing surface freshwater fluxes. *Climate Dynamics*, *43*(3), 709–736. https://doi.org/10.1007/s00382-014-2131-7

Sodemann, H., Weng, Y., Touzeau, A., Jeansson, E., Thurnherr, I., Barrell, C., et al. (2024). The cumulative effect of wintertime weather systems on the Ocean mixed-layer stable isotope composition in the Iceland and Greenland Seas. *Journal of Geophysical Research: Atmospheres*, *129*(19), e2024JD041138. https://doi.org/10.1029/2024JD041138

Solidoro, C., Bastianini, M., Bandelj, V., Codermatz, R., Cossarini, G., Melaku Canu, D., et al. (2009). Current state, scales of variability, and trends of biogeochemical properties in the northern Adriatic Sea. *Journal of Geophysical Research*, *114*(C7), 7–91. https://doi.org/10.1029/2008JC004838

Stewart, K. D., & Haine, T. W. N. (2016). Thermobaricity in the transition zones between alpha and Beta Oceans. *Journal of Physical Oceanography*, *46*(6), 1805–1821. https://doi.org/10.1175/JPO-D-16-0017.1

Sundby, S., & Drinkwater, K. (2007). On the mechanisms behind salinity anomaly signals of the northern North Atlantic. *Progress in Oceanography*, *73*(2), 190–202. https://doi.org/10.1016/j.pocean.2007.02.002

Sverdrup, H. U. (1950). Physical oceanography of the North Polar Sea. *Arctic*, *3*(3), 178–186. https://doi.org/10.14430/arctic3965

Tamura, T., & Ohshima, K. I. (2011). Mapping of sea ice production in the Arctic coastal polynyas. *Journal of Geophysical Research*, *116*(C7), 168. https://doi.org/10.1029/2010JC006586

Våge, K., Moore, G. W. K., Jónsson, S., & Valdimarsson, H. (2015). Water mass transformation in the Iceland Sea. *Deep Sea Research Part I: Oceanographic Research Papers*, *101*, 98–109. https://doi.org/10.1016/j.dsr.2015.04.001

Vesanto, J., & Alhoniemi, E. (2000). Clustering of the self-organizing map. *IEEE Transactions on Neural Networks*, *11*(3), 586–600. https://doi.org/10.1109/72.846731

Vilibić, I., Mihanović, H., Šepić, J., & Matijević, S. (2011). Using self-organising maps to investigate long-term changes in deep Adriatic water patterns. *Continental Shelf Research*, *31*(6), 695–711. https://doi.org/10.1016/j.csr.2011.01.007

Wang, W., & Huang, R. X. (2004). Wind energy input to the Ekman layer. *Journal of Physical Oceanography*, *34*(5), 1267–1275. https://doi.org/10.1175/1520-0485(2004)034⟨1267:WEITTE⟩2.0.CO;2

Xia, X., Hong, Y., Du, Y., & Xiu, P. (2022). Three types of Antarctic intermediate water revealed by a machine learning approach. *Geophysical Research Letters*, *49*(21), e2022GL099445. https://doi.org/10.1029/2022GL099445

Zhou, S., Meijers, A. J. S., Meredith, M. P., Abrahamsen, E. P., Holland, P. R., Silvano, A., et al. (2023). Slowdown of Antarctic Bottom Water export driven by climatic wind and sea-ice changes. *Nature Climate Change*, *13*(7), 701–709. https://doi.org/10.1038/s41558-023-01695-4